Validation of IPO: S-duct cavity

ERIK ZDANSKY, JONAS RAHM, ANDERS ÖRBOM,
MAGNUS GUSTAFSSON AND MAGNUS HERBERTHSON

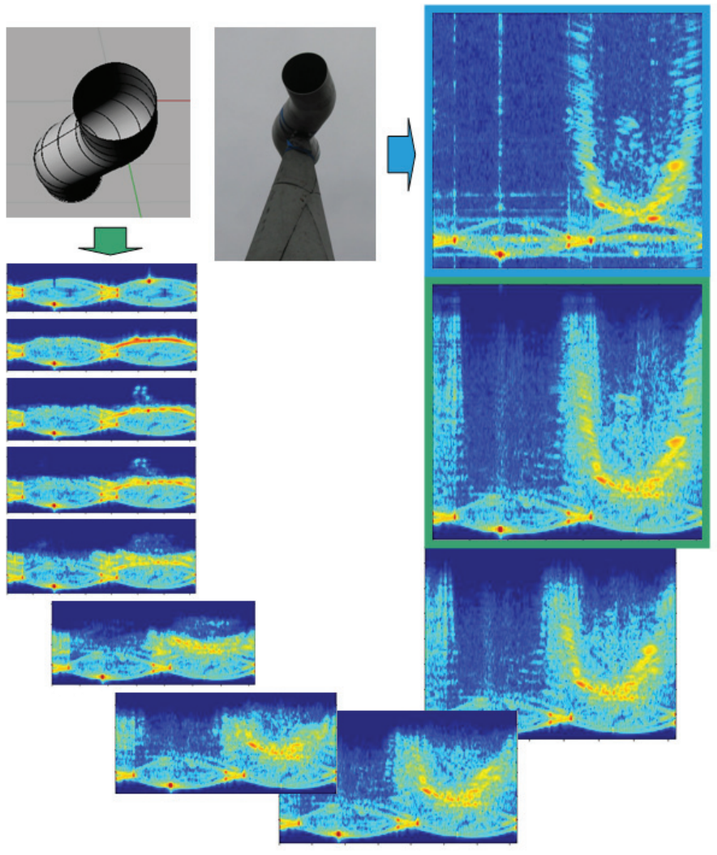

FOI, Swedish Defence Research Agency, is a mainly assignment-funded agency under the Ministry of Defence. The core activities are research, method and technology development, as well as studies conducted in the interests of Swedish defence and the safety and security of society. The organisation employs approximately 1000 personnel of whom about 800 are scientists. This makes FOI Sweden's largest research institute. FOI gives its customers access to leading-edge expertise in a large number of fields such as security policy studies, defence and security related analyses, the assessment of various types of threat, systems for control and management of crises, protection against and management of hazardous substances, IT security and the potential offered by new sensors.

FOI
Defence Research Agency
Information Systems
P.O. Box 1165
SE-581 11 Linköping

Phone: +46 13 37 80 00
Fax: +46 13 37 81 00

www.foi.se

FOI-R--3178--SE Technical report
ISSN 1650-1942 March 2011

Information Systems

Erik Zdansky, Jonas Rahm, Anders Örbom,
Magnus Gustafsson and Magnus Herberthson

Validation of IPO:
S-duct cavity

Title	Validation of IPO: S-duct cavity
Titel	Validering av IPO: S-kanalskavitet

Report no /Rapportnr	FOI-R--3178--SE
Report type Rapporttyp	Technical report Teknisk rapport
Pages/Sidor	46 p/s
Månad/Month	March/mars
Year/Utgivningsår	2011
ISSN	ISSN 1650-1942
Kund/Customer	FMV, FM
Kompetenskloss	Sensor- och signaturteknik
Projektnr/Project no	E53342, E3094 & E53349
Godkänd av/Approved by	Lars Bohman

FOI, Totalförsvarets Forskningsinstitut	FOI, Swedish Defence Research Agency
Avdelningen för Informationssystem	Information Systems
Box 1165	P.O. Box 1165
581 11 Linköping	SE-581 11 Linköping

Summary

Iterative physical optics (IPO) calculations of radar cross section (RCS) have been made on a medium size S-duct cavity for the purpose of benchmarking the method. Reference data has been collected by measuring a physical model of the cavity. The general agreement between the two data sets and derived results like range profiles and ISAR images is good. The method reproduces features whose apparent range indicate that they must be generated though quite complex scattering processes. With the run parameters used (relaxation parameter α_{rel}=0.6 and facet size less than half a wavelength) the method appears to converge safely in the present case. Cancellation of contributions from hidden facets appears to be fast, but results corresponding to complex scattering paths do require many iterations. Range profiles and ISAR (inverse synthetic aperture radar) images show some noise-like intensity not present in the measured data. However, the intensity level is rather low. It is tentatively suggested that it is due to "cancellation hum".

Work done on improving the IPO code and other software include better options for saving intermediate results, improved iteration speed, better storage of parameter settings, software for CAD and result conditioning. Several of the changes were made to meet immediate needs and would need additional work.

One particular advantage of IPO is the possibility to perform calculations which would be too large to address with e.g, MoM (the Methods of Moments). Although MoM can be expected in general to produce more reliable results than IPO, objects such as the cavity studied in this report could not be easily examined with MoM as the memory requirements and computing time would be unreasonable. The results produced by IPO, are not only easily achieved, and they are also encouragingly good. IPO might also be applied to electromagnetic problems other than radar cross section with advantage.

The upper frequency or object size (area) is not limited by the IPO method itself but by calculation time, and in the present implementation also by memory. Hardware and software developments including the use of efficient, compiled codes written in e.g. Fortran or C, could allow significant increases in speed and drastically raise the permissible number of facets. Unfortunately the time and in some cases memory demands grow with the fourth power of the frequency, for a fixed object size. If it would be possible to find algorithms permitting larger facets the practical object size limit would increase roughly in proportion to the facet size making such an advance valuable. One possible option for such development is discussed, but more work would be needed to investigate its feasibility. Another possibility is to hybridise IPO with other methods.

Keywords: IPO, iterative physical optics, benchmark, radar, RCS, X-band, Lilla Gåra

Sammanfattning

Beräkningar av radarmålyta (RCS) har gjorts med iterativ fysikalisk optik (IPO) på en medelstor S-kanalskavitet i syfte att testa metoden. Referensdata har erhållits genom radarmätningar mot en modellkavitet. Den allmänna överensstämmelsen mellan de två datauppsättningarna och därur erhållna avståndsprofiler och ISAR-bilder är god. Metoden reproducerar spridningsbidrag vars skenbara avstånd visar att de måste uppstå genom komplexa spridningsprocesser. Med använda körparametrar (relaxationsparameter α_{rel}=0,6 och fasettstorlek mindre än en halv våglängd) verkar metoden konvergera stabilt i det aktuella fallet. Målareabidrag från dolda fasetter tycks släckas ut relativt fort, men resultat som motsvarar komplexa spridningsvägar kräver många iterationer. Avståndsprofiler och ISAR-bilder (invers syntetisk aperturradar) visar en del brusliknande bidrag som inte har sin motsvarighet för mätdata. Intensiteten är dock relativt låg. En preliminär gissning är att det rör sig om ”kancelleringsbrum”.

Arbete för förbättring av IPO-koden och annan mjukvara innefattar bättre möjligheter att spara delresultat, ökad snabbhet, bättre lagring av körparametrar och mjukvara för CAD- och resultatprocessning. Flera av ändringarna gjordes för att möta omedelbara behov och kan kräva ytterligare arbete.

En särskild fördel med IPO är möjligheten att göra beräkningar för problem som skulle vara alltför stora att angripa med t.ex. momentmetoden (MoM). MoM kan visserligen i allmänhet förväntas ge bättre resultat, men t.ex. för den här studerade kaviteten skulle åtgången på minne och tid bli orimligt stor. De resultat som erhållits med IPO är inte lätta att uppnå och de är också uppmuntrande goda. IPO kan också tänkas ge fördelar vid andra elektromagnetiska beräkningar av annat än radarmålarea.

Vid IPO-beräkningar begränsas inte den högsta frekvensen eller största objektstorleken (ytan) av metoden i sig utan av beräkningstiden, och i denna implementering även av tillgängligt minne. Utvecklingen inom hård- och mjukvarusektorn inklusive möjlig användning av effektiv, kompilerad, kod skriven i t.ex. Fortran eller C, kan väsentligt öka beräkningshastigheten och tillåta en stor ökning av antalet modellfasetter. Olyckligtvis växer tidåtgången och i vissa fall även minnesåtgången med fjärde potensen på frekvensen vid konstant objektstorlek. Om man kunde finna metoder som medger en väsentlig ökning av fasettstorleken skulle objektet kunna få öka i storlek ungefär lika mycket vilket skulle vara ett värdefullt framsteg. En möjlighet till detta diskuteras kort men mer arbete krävs för att utröna om det är en framkomlig väg. En annan möjlighet att bearbeta större problem vore att hybridisera IPO med andra metoder.

Nyckelord: IPO, iterativ fysikalisk optik, benchmark, radar, X-band, Lilla Gåra

Content

1 Introduction

There exist a number of numerical methods to solve electromagnetic wave propagation problems, i.e., to solve Maxwell's equations with suitable boundary conditions and excitation. The three main principles to solve the Maxwell's equations are to put them into:

- an integral formulation (used in the Method of Moment, MoM, also called the Boundary Element Method, BEM)
- a variational formulation (used in the Finite Element Method, FEM)
- a finite difference approximation (used in the time domain it is referred to as the Finite Difference Time Domain method, FDTD)

These methods have their pros and cons which makes them to some degree interchangeable but also complementary. There exist hybrids of these methods, i.e., more than one method is used for solving a problem. For example the FEM method can be used to resolve some fine structure in a large scale problem for which the MoM or FDTD-method is used. The solutions in the different parts of the domain have to be coupled to provide the desired solution. However, they have one drawback, large computational domain (in comparison with the wavelength) they require large memory allocations and correspondingly long run times which makes them not useful in some cases.

In high frequency cases (when the wavelength is much smaller than the typical geometry variation in the object) one can simplify the Maxwell's equations to geometric optics (GO), or physical optical (PO) approximations. An alternative approach is the Iterative Physical Optics (IPO) method which is a modification of an integral formulation of the Maxwell's equations which is solved iteratively, supplemented with certain shadowing conditions [1-5]. It is a relatively fast and less memory demanding than the full wave solvers, and it is more exact than the standard high frequency methods.

This report present a validation of an IPO code developed at FOI. Comparisons between IPO computations of the radar cross section (RCS) for an S-shaped cavity with measurements have been performed. In addition, ISAR and down-range images from calculations and measurements have been compared and the agreement is good.

The work has been sponsored by the Swedish Armed Forces and the Swedish Defence Material Administration (FMV).

2 IPO-calculations

The presently used algorithm and implementation of IPO (iterative physical optics) is described in [6]. IPO is also discussed in [7] and a previous application of IPO to a similar cavity has been reported by Burkholder and Lundin [5]. For a treatise of the theory and the history of IPO the reader is referred to [1-7] and references therein.

The method is basically derived as a recursive solution to the magnetic field integral equation (MFIE). Very briefly the basic algorithm may be described as calculation of initial facet surface current densities (often just referred to as "currents") for the incident illumination followed by iterations to find current densities satisfying the MFIE and, finally, calculation of the scattered field from these current densities. In the iterations coefficients are used to describe the relation between current densities on different facets. In this implementation the coefficients are stored in "A-matrices". However direct recursive solutions of the MFIE will often not converge and IPO refers to a set of modifications introduced for the purpose of convergence[1].

The main attraction of the method lies in the fact that the method is fairly accurate, simple, fast and, in particular, suitable for an object size range intermediate between high frequency methods like PO/GO, and accurate, "exact", methods like the method of moments (MoM), which suffer from severe problem size restrictions. Also, once the surface current densities have been found through iteration the bistatic cross section can easily be calculated for any scattering direction. Furthermore, in some respects, the method put less demands on the CAD mesh.

One disadvantage with IPO is that in certain cases the current densities of some facets will never be affected by the iterations and then only contribute according to the physical optics (PO) approximation for single scattering. However, in most such cases this is likely to be a fair approximation.

This work has used an IPO implementation written in MatLab [6]. MatLab is efficient in handling large arrays of data but since it uses an interpreter the execution of many lines of code e.g. in loops is less efficient. It is thus suitable for matrix formulations of the IPO algorithm meaning that the problem size is typically limited by the memory available. Other algorithm implementations exist that are claimed to be highly memory efficient at a not too severe speed penalty if compiled code is used [5]. Compiled codes are also likely to be better suited for removing geometries with fast convergence from further iterations in order to improve speed. However, even in compiled code, the benefits of convergence evaluation must be weighed against its cost [5]. In the present implementation four complex matrices ("A-matrices") are used to describe the coupling between the surface current elements (facets of the CAD model). With n_p facets each matrix will have n_p^2 elements. The edge-length of a square facet may typically be up to $\lambda/3$ or $\lambda/2$ [5-7], but these are not sharp limits. The number of facets thus increases with the square of the radar frequency (or rather the frequency on which the faceting of the CAD model is based, i.e. typically the highest frequency for which calculations are to be made) and the size of the matrices with the square of the number of facets i.e. with the fourth power of the frequency. The processing time will depend on the time needed for filling the matrices and the time needed for performing the iterations. The time needed for filling the matrix will depend largely on the number of elements, i.e. f^4. The iteration time will largely depend on the time needed for matrix multiplication (f^4) but also on processes more dependent on the number of facets (f^2).

The use of this facet size has, at least partly, been established empirically, but it is evidently closely related to the sampling theorem. It may be surprising that it is possible to approach $\lambda/2$ so closely. The reason is probably that in many geometries the phase velocity is

[1] In particular the equations are modified so that the solution is technically not a solution to MFIE but to a related set of equations.

considerably higher than the group velocity i.e. due to projection effects the phase usually varies more slowly across the surface giving better sampling margin.

The memory required by MoM also grows with f^4 but for the same object size and frequency it will require much more. It typically uses facets of size λ/8 or smaller meaning that n_p increases by a factor 16 and n_p^2 by a factor of 256. It also needs to handle all facet edges increasing the memory demand even further. When it comes to speed the situation is even worse since there are that many more facets to process and in particular since the processing time grows with f^6.

Some modifications have been made to the previous FOI matrix IPO implementation. The main changes are improved possibilities to save intermediate results and input parameter settings and modification to improve speed. Previously the result was only calculated in "far-field amplitude" units, or as surface currents for further processing, but an option to directly obtain "scattering amplitude", $\overline{S}$, for which $\sigma = |\overline{S}|^2$ was added. Flags have been introduced to define which quantities that should be calculated or saved. Code for generating the calculation flags from the save flags according to the sometimes somewhat complex default dependencies has been added for convenience and for avoiding time-consuming mistakes. Some work has also been made on implementing free space aperture grids, but stringent theoretical rules for the use of them would be needed. The handling settings, previously done through a combination of parameters in the CAD files and through function input parameters has been replace by an initial hardcode section in the main program. This is more convenient and better suited for future development of a GUI (graphical user) interface. A function has been written to automatically collect all parameters at the end of this input section and save them for documentation. Much code has also been written for the purpose of CAD preparation and result evaluation. Some of this is of temporary character while other programs will be useful tools for future work but may require further development. The forward-backward method of Burkholder and Lundin [5] has been studied. It has not been implemented but this would be easy to do.

The derivation of the MFIE requires the calculation grid to be closed, i.e. the object should be bounded by surfaces with normals facing outward in all directions, and the resulting signal is calculated from the currents on all these surface elements. Objects may be physically thin, i.e. the front and back of a plate may lie in the same plane, but in the present implementation the front and back elements must then not be chosen so that they have the same centres of gravity since this would give singularities in the matrices. In [5] the cavity used was closed by the use of a free-space grid covering the aperture. The advantage of this is that the cavity signature calculated does not include contributions from the outside and that the size of the problem is reduced.

It may seem paradoxical that currents well shrouded for the receiving antenna would be important for the result, but the current densities solving MFIE have the properties of giving contributions cancelling each other where the net result should be small, and if it converges IPO finds this solution. This eliminates the cumbersome tracing of shadows and its GO approximations, which is certainly one of the strengths of IPO. Unfortunately this also makes the current distribution is difficult to interpret intuitively.

Despite the requirement for a closed grid it is sometimes possible, at least in some radar geometries, to obtain good results for objects that are not closed. For example it was found that all elements not facing forward could be dropped from the CAD model of a dihedral without any degradation within the open sector of the dihedral. Also rough surfaces have been previously been calculated using much larger elements on the back side without any adverse effects [6].

The interior and exterior of the S-duct appear to be well separated in the sense that no real, physical, rays hitting the exterior is likely to scatter into the interior and vice versa, suggesting that it would be possible to treat them separately. This, and also the use of larger

outside elements were tested. The result was at best approximate but with obvious deviations and this was not further pursued. Probably the reason for failure in this case is incorrect cancellation of certain contributions while the reason for success in the cases mentioned above is that there are no, or only very weak, currents on the surfaces that were formally not correctly handled.

2.1 The cavity CAD

A previously generated CAD model was available. It has the dimensions of the S-duct used for measurements. The exterior, however, had been idealized having a fixed flat bottom instead of the lid of the model used for measurements, see figure 1.

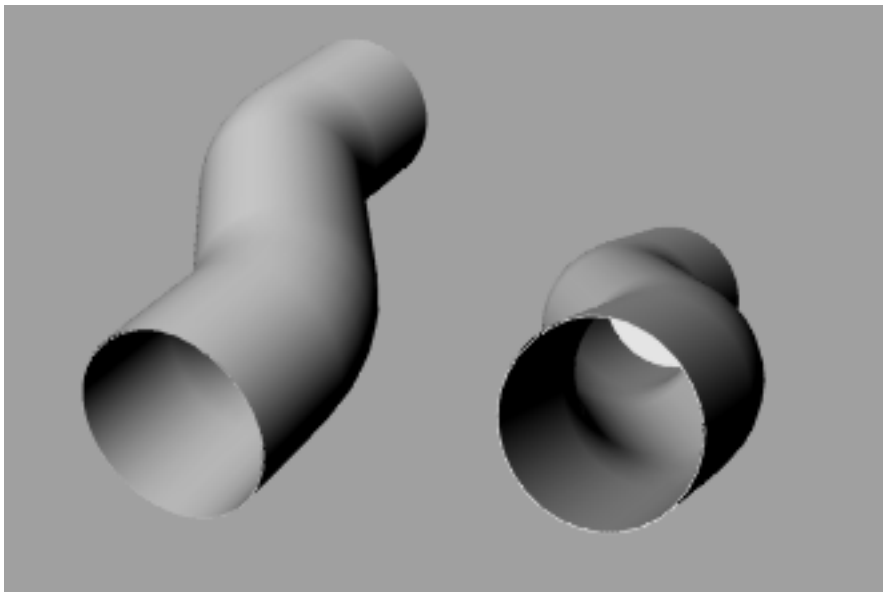

Figure 1. CAD model of the S-duct cavity. Inside diameter 300 mm *length 1200* mm*. Please refer to figures 3 and 4 in the measurement section for more details.*

This CAD-model was implemented as a `.3dm` CAD-file in the Rhinoceros CAD-software. In this file it is represented using medium-level primitives, such as cylinders. For the purpose of IPO calculations the CAD model needs to be exported to a facet-based format, in this case `.raw`, i.e. raw triangles. The Rhino export GUI permits some control of the faceting through a number of control parameters. Unfortunately, Rhino seems to apply these rather approximately. Due to this and other limitations it does not provide a very satisfactory command of the faceting requiring the merging of adjacent facets and assembly of parts from different `.raw`-files in order to generate geometry sets useful for the IPO-calculations. It is also important to check and correct the sign of facet normals.

It was found necessary to modify the bottom in the CAD-merging procedure. The resulting bottom was physically thin, but after adjusting so that the centres-of-gravity on the inside and the outside did not coincide this worked fine.

At first a $\lambda/3$ faceting limit was applied to the longest edge of the .raw triangles, i.e. to the diagonal of the corresponding rectangles (Rhino typically uses simple rectangular facets, in the .raw format these are split into triangles which were later rejoined in order to keep the model size down). It was found, based on these assumptions, that a model with 21328 facets requiring 14.6 GB of memory for the A-matrices could be generated that should be valid up to 5 GHz. Later a 43266 facet model valid up to 9 GHz was generated requiring 60 GB of memory, intended for a computer with 72 GB of RAM was generated. Attempts to run this model indicated that the load was too heavy for the computer. Probably the computer started swapping memory resulting in very low speed, but even in the absence of swapping a

calculation time increase of $(43.3/21.3)^2 \approx 4.1$ must be expected which would have been too much in this case. However, it was noticed that Burkholder and Lundin [5] do not apply this limit to the largest facet dimension but give the rule as 4 to 9 facets per λ^2. If the facets are assumed to be square the longest diagonal of $\lambda/3$=11 mm would then give an edge length of $\left(11/\sqrt{2}\right)$mm=$\lambda/2$ at 9.64 GHz. In reality the longest diagonals were somewhat shorter permitting frequencies slightly above 10 GHz if the assumption of square facets is correct. The present calculation indicates that the smaller model (21328 facets) does indeed work slightly above 10 GHz while tests at 11 GHz shows serious breakdown.

2.2 Calculation settings

The calculations were made for 0 to 360º in 0.4º steps (901 angles) azimuths in the symmetry plane of the cavity, see figure 6. The frequency was 7.992 to 10.008 GHz in 16 MHz steps (127 frequencies) for HH polarisation. The numerical precision was "single". These settings were used to obtain high spatial resolution in the data analysis through the use of range profiles and ISAR images. The values were chosen on the basis of available measurement data, demands on resolution and unambiguity, memory and time available for computation and the useful frequency range of the faceted CAD models prepared. This gives a range resolution of 75 mm, the unambiguity distance is 9.37 m in downrange and 2.39 m in crossrange. The object and its ambiguous images will then be well separated in cross-range and most of the multiple scattering tail will fall within the downrange unambiguity distance leaving only its weakest tip to be overlapped.

Based on tests the relaxation parameter $\alpha_{\mathbf{rel}}$=0.6 and 70 iterations were used. A larger value gives faster but less reliable convergence. The tests indicated some of the cavity features only started to show up after dozens of iterations, and as we will see from the results the cavity tails may not be fully developed after 70 iterations.

2.3 Calculation time

The calculations were run using three MatLab processes on two computers. When running alone on one computer the calculation of all 901 angles for one frequency typically takes 4h05min. With 127 frequencies run sequentially on one computer this would give a total time of 21d15h. Although the filling of the matrices take 7 min the number of iterations used will quickly make them take the major part of the calculation time (typically 3min25s/iteration). These figures include the times taken to calculate and store intermediate results (9KB scattering amplitude files, matrix filling time includes primary illumination and 0:th iteration result). However, if scattering amplitudes were only calculated for the last iteration it should be possible to save some of this time.

2.4 Convergence in the calculations

During calculations convergence is probably best tracked using quantities based on changes in the surface current densities as done by Burkholder and Lundin [5]. Convergence is presently not included in the MatLab IPO implementation [6] so that convergence analysis must be made after the calculations. Intermediate current density results may be saved, but this takes a lot of disk space and is very slow leaving us with the option of using calculated scattering amplitudes for the analysis.

Figure 2 shows a diagram of the RCS incoherently averaged over all calculated frequencies. This diagram gives an overview but diagrams showing various differences for individual frequencies would, of course, provide more sensitivity.

The contributions from facets after directly after primary illumination (iteration 0) should correspond to PO results for the same illumination. PO is known to provide reasonably accurate results objects larger than a few wavelengths if illumination is correctly described. For convex objects self-shadowing would be sufficient to describe illumination, but for cast shadows and secondary illumination PO codes would use supplementary methods like GO (ray-tracing). In this case multipath propagation must be expected to be of minor importance for the exterior of the cavity so that the contribution from primary illumination of the exterior surfaces should be nearly correct. However with only self-shadowing applied interior cavity surfaces will also be illuminated giving incorrect contributions making these hidden surfaces visible in range profiles for the 0^{th} iteration (see range profiles in the appendix). As also seen in the appendix the first few iterations surprisingly quickly attenuate or redistribute these currents so that these contributions are cancelled and the convergence in the range 0 to 180º is fast (figure 2). Even over much of the 180 to 360º range, where the cavity aperture is illuminated, convergence appears to be good well before the 15^{th} iteration as reported by Burkholder and Lundin [5], but in the cavity region some peaks start growing only after 10, 30 or even more iterations, which is not surprising since they correspond to beams bouncing back and forth many times in the cavity and the relaxation parameter delays their growth in the calculations.

As already referred to, the convergence may be followed in more detail in the diagrams in the appendix where it is clear that it takes time for the multipath "tails" to grow and that they continue growing even under conditions where it is impossible or very difficult to see any changes in figure 2. In fact, the tails would probably continue to grow past 70 iterations even though they represent so little energy that changes could be difficult to follow in a RCS(f,φ) diagram.

In many cases it not be necessary to reproduce the full length of weak multipath tails and in same cases not even to obtain accurate RCS values as long as the average over the radar band and some angular range, over which the evaluation is made, are correct within the precision required. Time could then be saved by using fewer iterations.

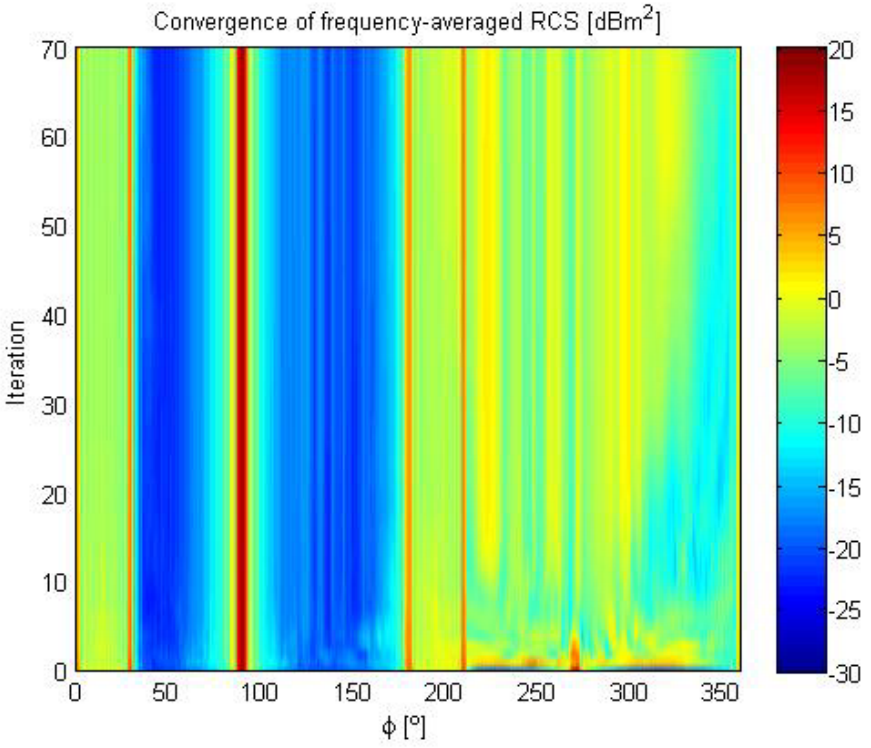

Figure 2. Convergence as followed by intensities incoherently averaged over the full calculation bandwidth. While giving a good overview this type of diagram does not provide very good sensitivity to convergence for individual frequencies.

3 RCS measurements on the cavity

3.1 The measurement model

The physical model cavity, which was originally constructed for an infrared study [8], is an open-ended S-duct equipped with a lid. The duct was made from prefabricated aluminium sections welded together. The welds and tube surfaces have to some extent been tidied up and smoothed by grinding after the welding operations. In order to close the cavity during the RCS-measurements a flat circular plate was inserted on the inside of the lid. Figure 3 depicts the shape and dimensions of the cavity. Figure 4 shows photos of the physical implementation of the cavity.

Radar cross section measurements on the cavity, were previously performed at the FOI outdoor facility 'Lilla Gåra' [9-10] during November 2009. For the infrared study the ends of the cavity were open and a special cover lid with a hole and some insulation material were used to seal one end. In the radar case, a circular aluminium plate was attached to the inside of this lid to form a flat cavity bottom.

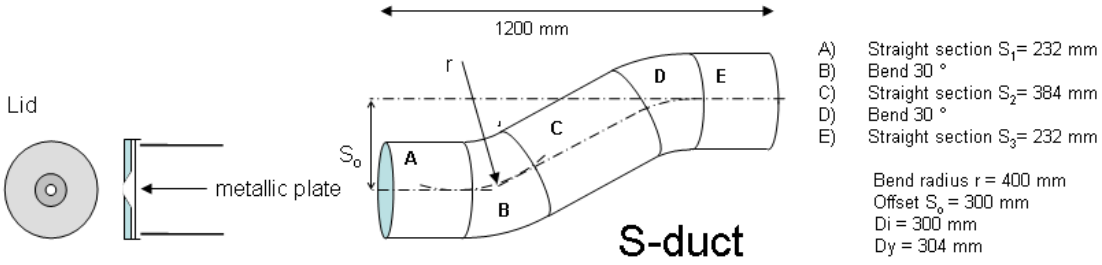

Figure 3. Dimensions of the S-duct.

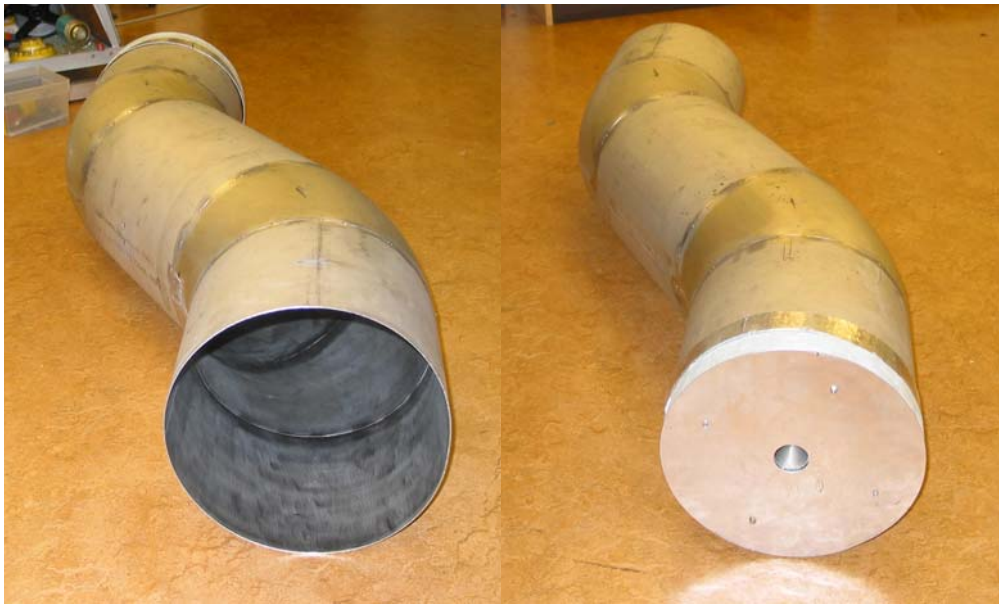

Figure 4. Photographs of the cavity from both ends.

Figure 5 and 6 show schematic sketches of the measurement setup and how the angles are defined for the measurements. The metallic plates in front of the turntable are used for screening by deflecting radar waves to shadow the pylon. This will reduce unwanted background contributions that can interfere with the total RCS of the object. The distance between the centre of the pylon and the parabolic antennas is 101 meter. The height from the ground to the centre of object and to the centre of the antennas was around 4 meters.

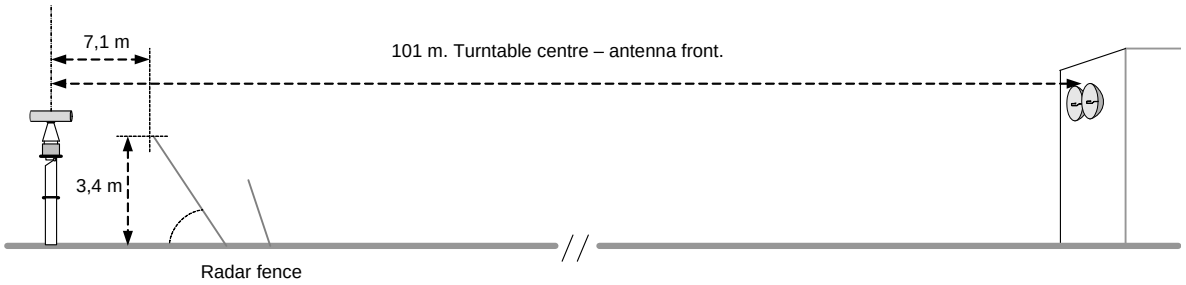

Figure 5. A sketch of the measurement setup from a side view.

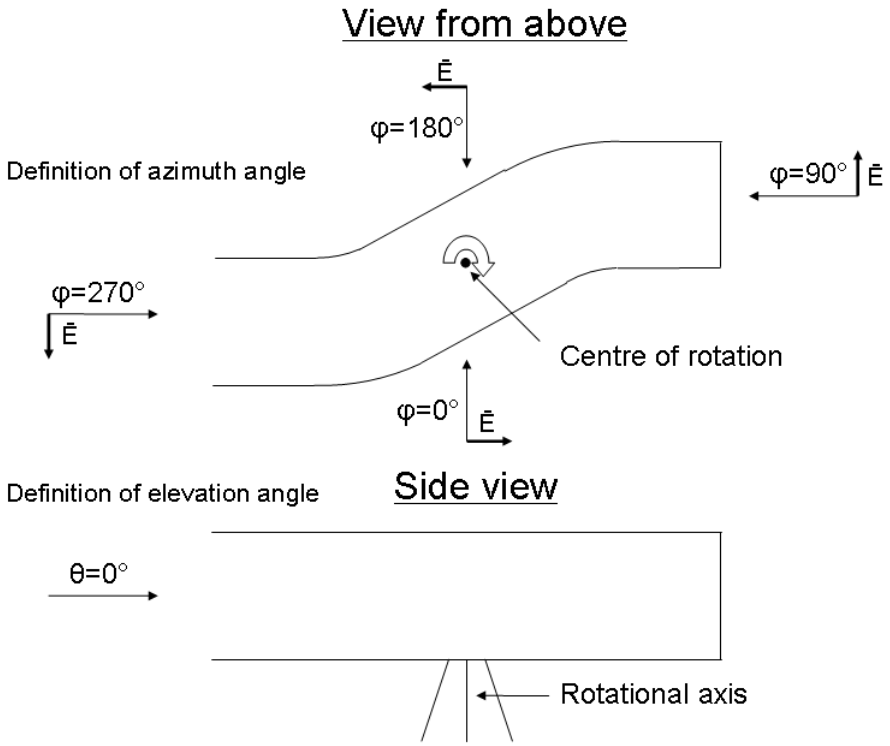

Figure 6. Schematic sketch of the cavity on the turntable. The rotation is made clockwise seen from above. The angle definitions are shown in the figure together with the definition of horizontal polarization vector Ē.

The cavity was placed on a support that is attached to the turntable, see figure 7. To stabilize the cavity during the measurements, the cavity was strapped to the support with textile ribbons, see figure 7. As we will see this support affects the RCS result somewhat, but the contributions can be rather well separated.

Figure 7.The upper left picture shows the support that is attached to the turntable. The upper right picture shows the cavity placed on the support and how the cavity is tied with a band to the support. The lower left picture shows a view of the setup from the antennas. The lower right picture shows the setup from behind the pylon. The two parabolic antennas that have been used can be seen between the ladder in the background.

3.2 Calibration

A flat circular plate was used as calibration object. The radius of the plate was 0.125 m giving a radar cross section of around 28 dBm^2 at 10 GHz. The maximum reflection response, i.e. the specular reflection, was found by rotating the turntable in small angular steps, both in azimuth- and elevation. When the specular position of the plate (relative the antennas) was found the response was measured as a function of frequency. To reduce unwanted contributions, originating e.g. from the background, range profiles were created for the calibration data and the calibrator contributions were gated before converting back to frequency domain. As will be discussed in section 4.1 errors in the measurements or the calibration give calibrated intensities that are too low.

3.3 Antennas

Antennas:	Parabolic antennas (4 feet in diameter)
Beam width:	~ 2° at 10 GHz which gives a 3 dB beam width of about 3,5 meters at the turntable position.

3.4 Measurement parameters

PRT: 10 µs

Pulse width: 500 ns

Delay: 1300 ns

Frequencies: 8 – 12 GHz in 4 MHz steps, i.e. 1001 frequencies.

Polarisation: Horisontal-horisontal, see figure 6 for definition.

Azimut angle: φ = 0° - 359.95° (see figure 6) in 0,05° steps, i.e. 7200 angles.

Elevation angle: θ = 0° (see figure 6)

3.5 Measurements results.

Figure 8 shows calibrated RCS curves for a few sample frequencies while figure 9 provides a colour coded map of the RCS for the full measured frequency range.

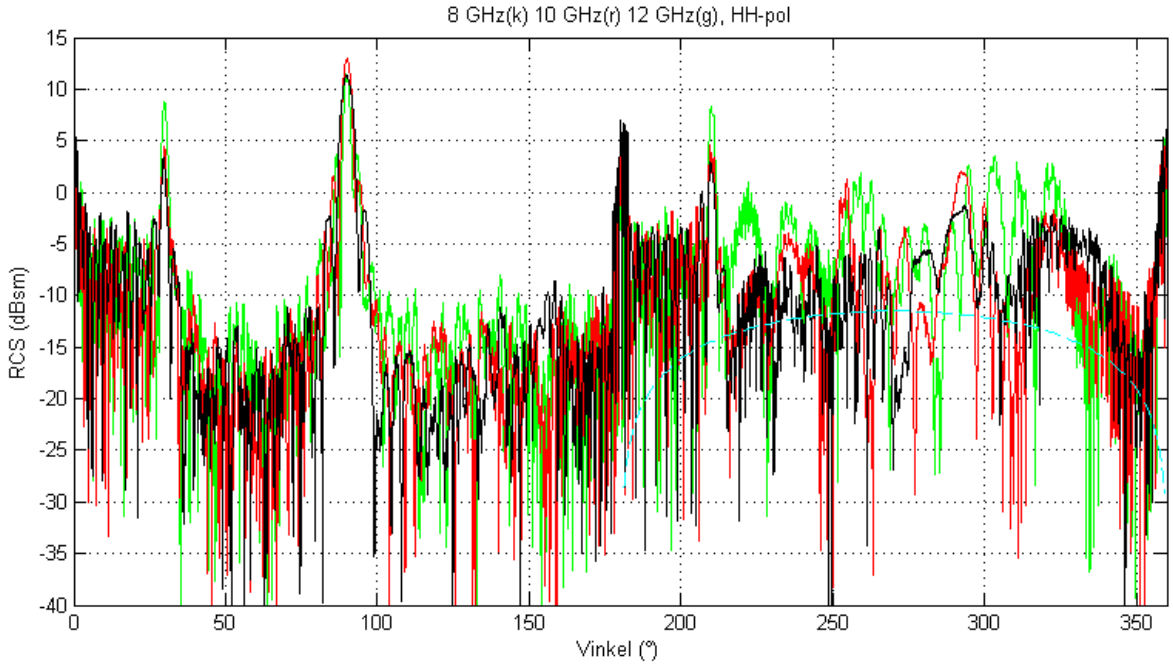

Figure 8. Measured radar cross sections as a function of angle for a few frequencies. The projected geometric area of the cavity aperture is indicated by the dashed light blue line.

In the range 180 to 360 degrees the radar illuminates the cavity aperture directly while outside this range it will only see the outer side of the object (including the small lid cavity) albeit edge diffraction might still lead to minor illumination of the interior cavity. Due to the S-shape of the cavity its interior will be more deeply illuminated in the 270 to 360º range than in the 180 to 270º range. In a real case, with a duct being part of a larger object the relation between the two quadrants is likely to be modified by other parts. In the range 270 to 297º parts of the cavity bottom are optically visible through the aperture so that direct illumination of parts deep within the cavity must be expected. Closer to 180 and 360º

respectively deep parts would only (in a GO picture) be illuminated after many bounces. As expected the RCS of the outside region is more concentrated into a few strong peaks with low intensities between them, but the doubly curved bends raises the levels in the ranges 0 to 30º and 180 to 210º and the RCS values in the cavity aperture region are typically of intermediate strengths.

The average RCS of a randomly scattering lossless cavity is expected to equal its projected geometrical entrance area [11]. In this case the average values appear to be significantly higher, see figure 8. The more likely explanation for this is that the re-entrant geometry of the cavity is not randomly scattering but has partly retroreflective properties. This may be compared with a lossless rectangular cavity, which in the GO approximation is strongly retroreflective. There will, of course, be contributions from outside parts in this region too, but as demonstrated by the range 0 to 180º these are typically lower.

The outside back end of the cavity is seen at 90º, and as expected the peak width decreases with frequency. The cylindrical sections A and E (figure 3) are seen at 0/360º and 180º. Due to interference between A and E the intensity of these peaks oscillates strongly giving them a multilobate appearance. In figure 9 the intensity is seen to vanish every 0.5 GHz corresponding to two equal scatterers at a distance of 0.3 m from each other, i.e. the S_0 offset in figure 3. The mid section C appears at 30º and 210º. These peaks also show a frequency-dependent intensity variation with a period of approximately 1.6 GHz, which is an artefact due to interference with the cylindrical part of the support.

In the range 210º to 310 or 330º the RCS appears to vary less rapidly with angle but more strongly with frequency than in the angular ranges dominated by the outside of the cavity.

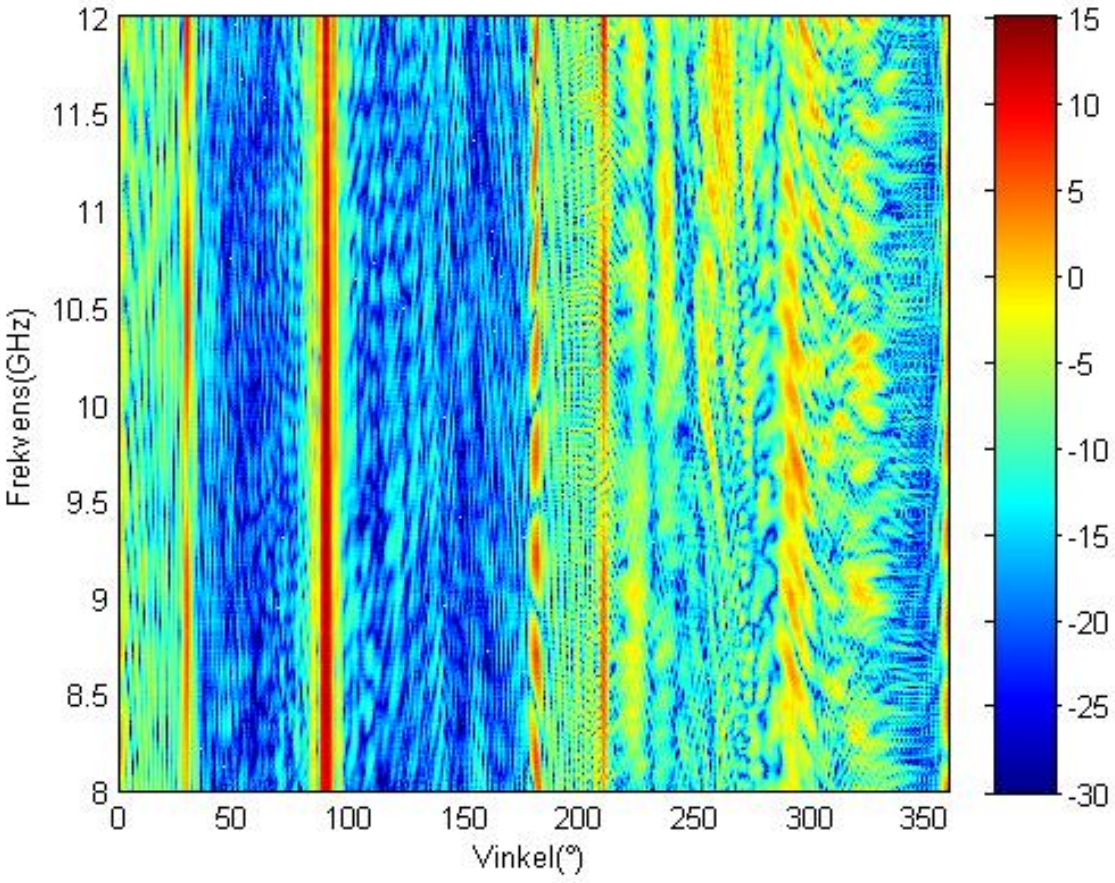

Figure 9. Measured RCS [dBm^2] *as a function of angle and frequency.*

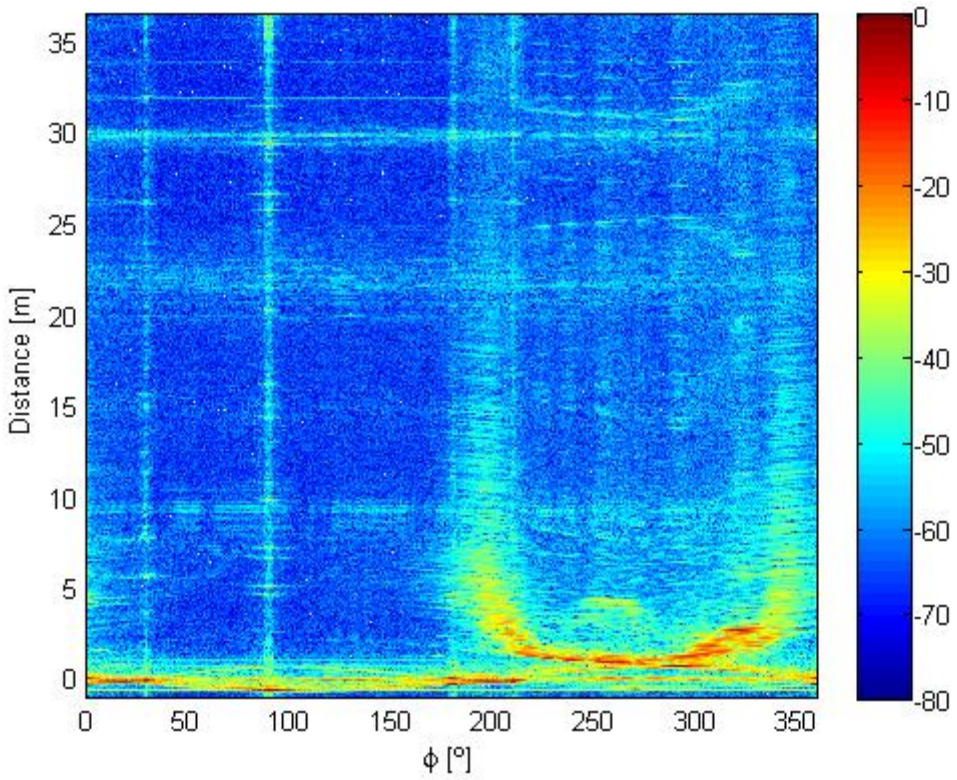

Figure 10. Downrange profiles calculated from measured data. Intensity scale in dB *(see footnote 2).*

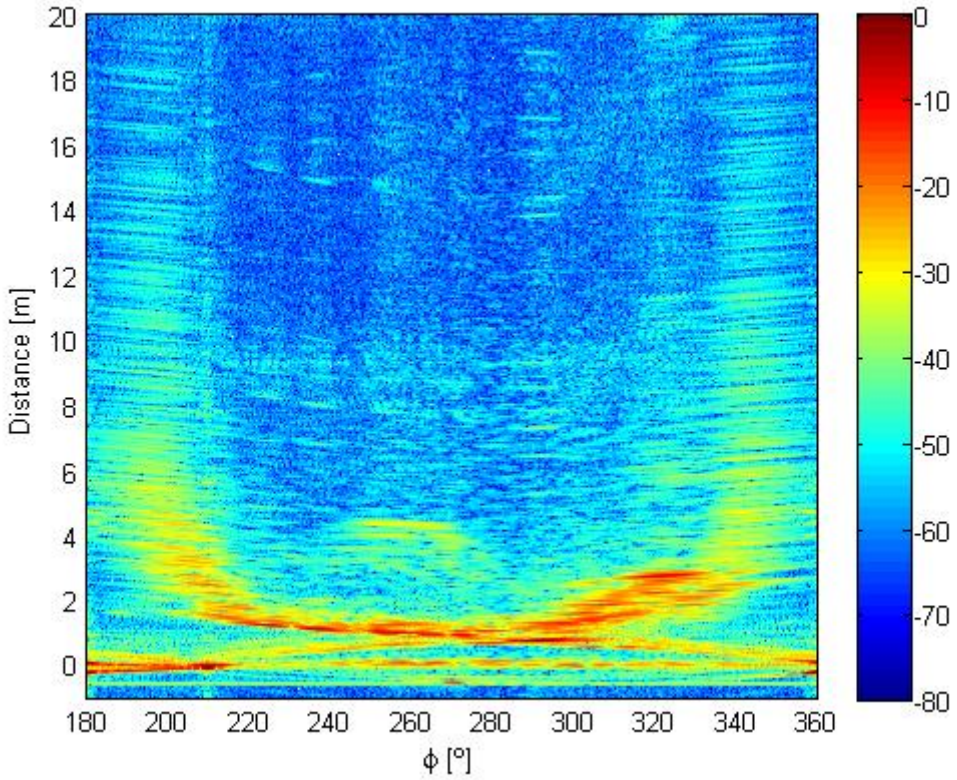

Figure 11. Close-up of the nominal cavity angular range. Intensity scale in dB *(see footnote 2).*

In order to gain a better understanding of the cavity properties it is of interest to generate down-range profiles and ISAR images[2].

In the overview image 10 the full unambiguous range is displayed. The main reflexes from the cavity walls can be seen together intensity plumes associated with multiple scattering in the cavity. In addition to this intensity leakages from the strong specular reflexes can be seen as vertical and horizontal bands and some weak ghosts due to non-idealities in the measurement system can be seen at large range.

The next image, figure 11, shows the range profiles down to 20 m in the cavity-aperture region.

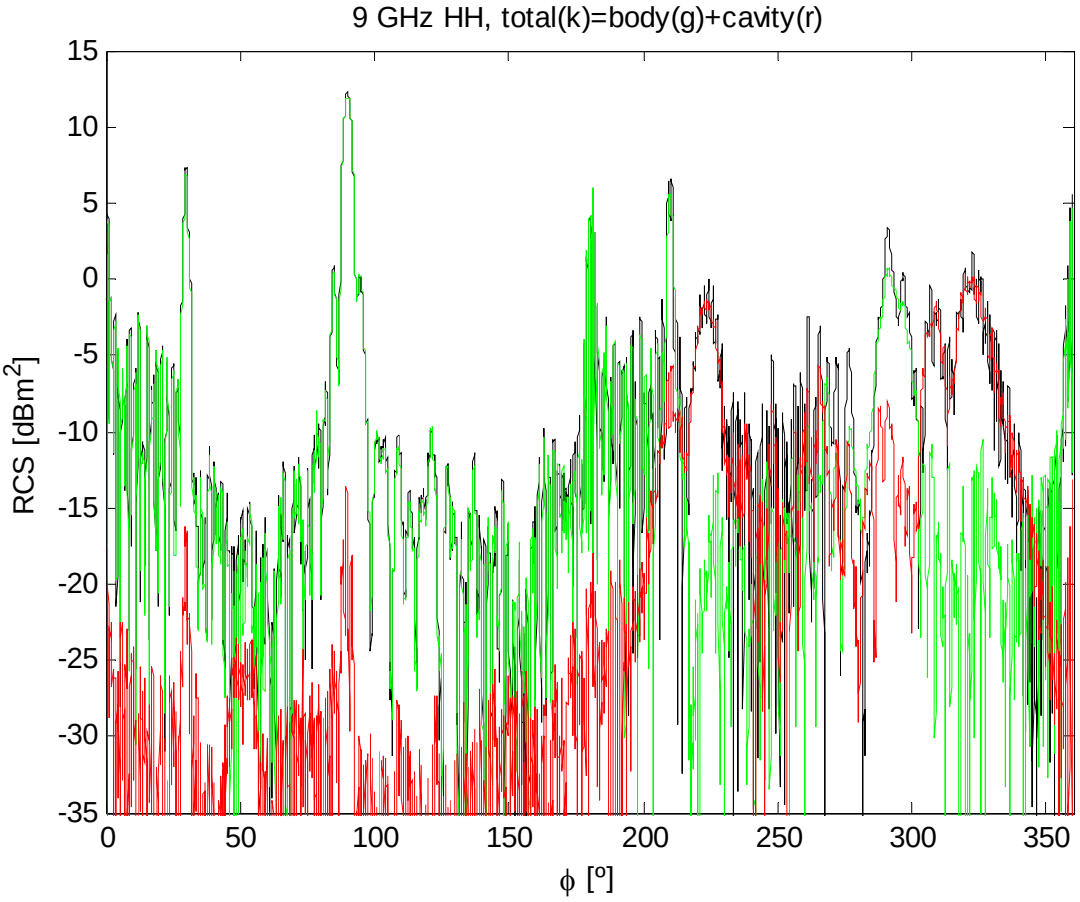

Figure 12. The total RCS (black) split into body (green) and cavity (red) contributions, as described in the text.

Figure 12 shows the results of a separation of the total RCS into "body" and "cavity" contributions by gating directly in the range profiles and inverting back into the frequency domain. One border was drawn close to 0.9 m in figure 11 placing essentially all direct

[2] In principle the linear power unit for RCS intensity in range profiles and ISAR images would be m^2/pxl or m^2/m=m and m^2/pxl or m^2/m^2 respectively. These values would represent sums or averages over the supporting data dependent on the processing used. In this paper a proper normalisation of the range profiles and the ISAR images for this processing gain has not been pursued and the colour scales in dB should thus only be interpreted as relative intensities. In the next section, 4, and the appendices, the range profiles for measured and calculated data will have nearly the same processing gain, but the intensities of the measured data are probably somewhat low. In the ISAR images the processing gains are different but the intensity scales have been qualitatively adjusted to compensate for this and all images have been drawn with the intensity log scale span.

reflexions, including those of the cavity, in the body part. The cavity part is dominated by the long cavity-related multiple-scattering plumes. Since the remote part of the plumes are quite weak and figure 10 indicates significant leakage of body intensity into other regions the other border was placed near 25.9 m making the body part wrap around. Of course, the region beyond this could have been excluded together with that before -0.6 m, but here a simple split of the total intensity into two parts was chosen. Despite this there are clearly body contributions to the red curve, but they do not really distract the picture. As evident already in the range profiles the cavity contributions are significant in the 200 to 340º range, but at 210º the contribution from section C dominates and around 295º direct, or nearly direct, contributions from the cavity bottom dominate. In the range 230 to 280º the cavity contributions are modest and not as dominant as might be expected. However, the body part in this range is likely to be exaggerated by erratic contributions from the support. The strongest cavity contributions appear in the 200 to 230º and 305 to 330º ranges. Of course, this figure illustrates an individual frequency, but conditions appear to be similar for other frequencies.

4 Comparison between calculations and measurements

4.1 RCS and range profiles

Figure 13 shows comparisons between measured and calculated results for a few frequencies. Figures 14-15 shows colour maps of the RCS as a function of both angle and frequency and figures 16-17 show the corresponding range profiles. The measurement data is a subset comprising only frequencies for which calculations are available, hence the unambiguity range is shorter and the resolution lower. Due to the differences in signal levels discussed below, the upper limits of the colour scales have been adjusted to emphasize the similarities between the calculated and measured results.

From figure 13 it is clear that the measured intensities are too low indicating some type of measurement or calibration error. The general agreement between the two data sets, however, appears to be fair. The bottom and the cylindrical parts of the object have some potential of being used as internal calibration objects. However, the bottom has a small cavity and is not quite flat, the mid cylindrical part will interfere with the cylindrical parts of the support and the end parts will interfere with each other. Furthermore there will always be some interference with other parts of the object, e.g. the bends which are partly very similar to the adjacent cylindrical parts. Gating in ISAR films could be used to separate these contributions and comparisons could be made with similarly gated results from calculated data in order to reduce gating effects.

In the low intensity regions between 0º and 180º the intensity levels are more equal and the measured results partly even exceed the calculated. This is interpreted as due to measurement background, in particular support structures.

In the range 0 to 30 and 180 to 210º the levels are enhanced due to specular scattering from areas on the doubly-curved sections B and D that are normal to the direction of incidence. Using dimensions as in figure 3 and an analytical PO-approximation [11] for the RCS of the convex outer bend surface would be $\pi 0.5 D_y (r+0.5 D_y)$ or -5.8 dBm^2. This will interfere with the contribution from the inner bend (-9.3 dBm^2) and possibly other sources leading to the rapid fluctuations. If added in phase these two contributions would give -1.3 dBm^2. roughly corresponding to the upper levels of the calculated curve in these ranges.

In the cavity range 180º to 360º the RCS variations are less rapid. The general agreement between measured and calculated data appears to reproduce less detail here. The complex scattering conditions in the cavity could probably lead to high sensitivity to minor deviations in geometry leading to such a discrepancy between measured and calculated data. One test for this hypothesis could be to do calculations on deformed cavities in order to investigate the sensitivity to such errors. As will be found below these differences are less prominent in the RCS(φ,f) diagrams, figures 14 and 15 and the high resolution results are in good agreement.

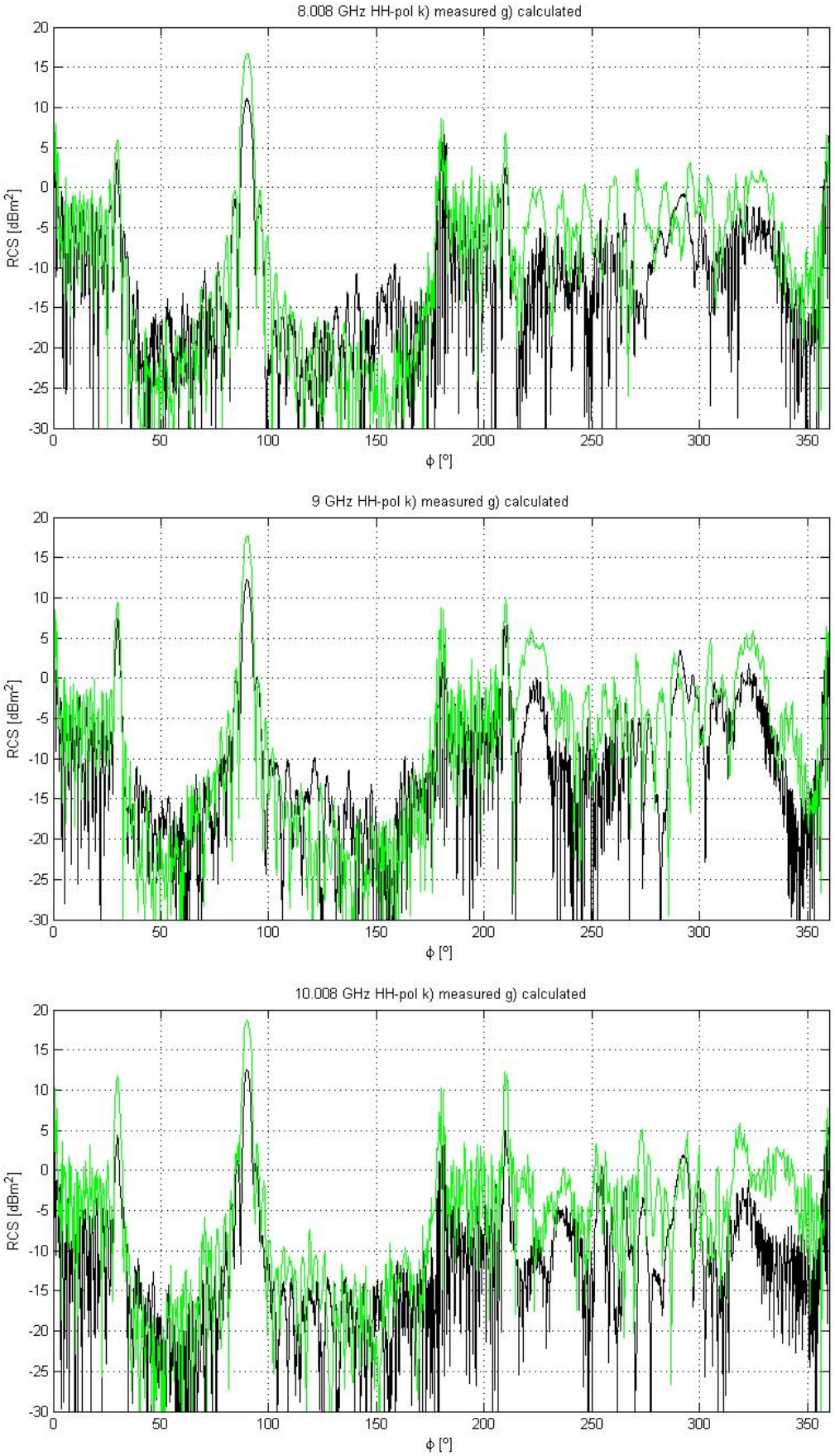

Figure 13. Comparison of calculated (green) and measured (black) radar cross sections for three frequencies.

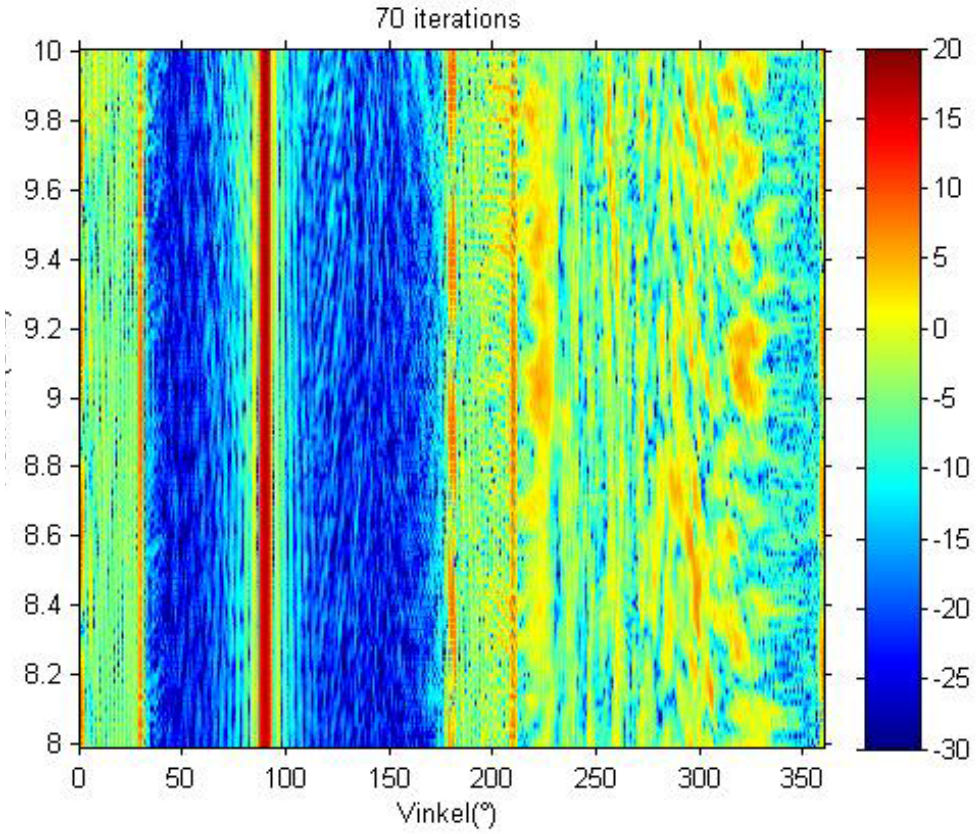

Figure 14. Calculated RCS [dBm^2] *as a function of angle and frequency*

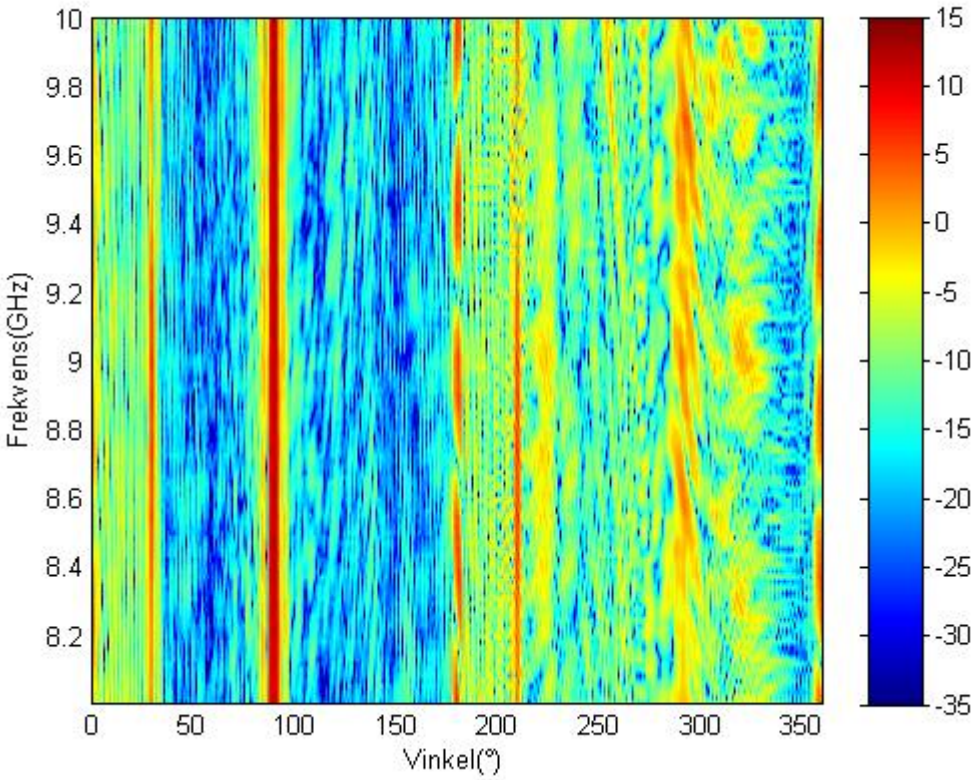

Figure 15. Measured RCS [dBm^2] *as a function of angle and frequency*

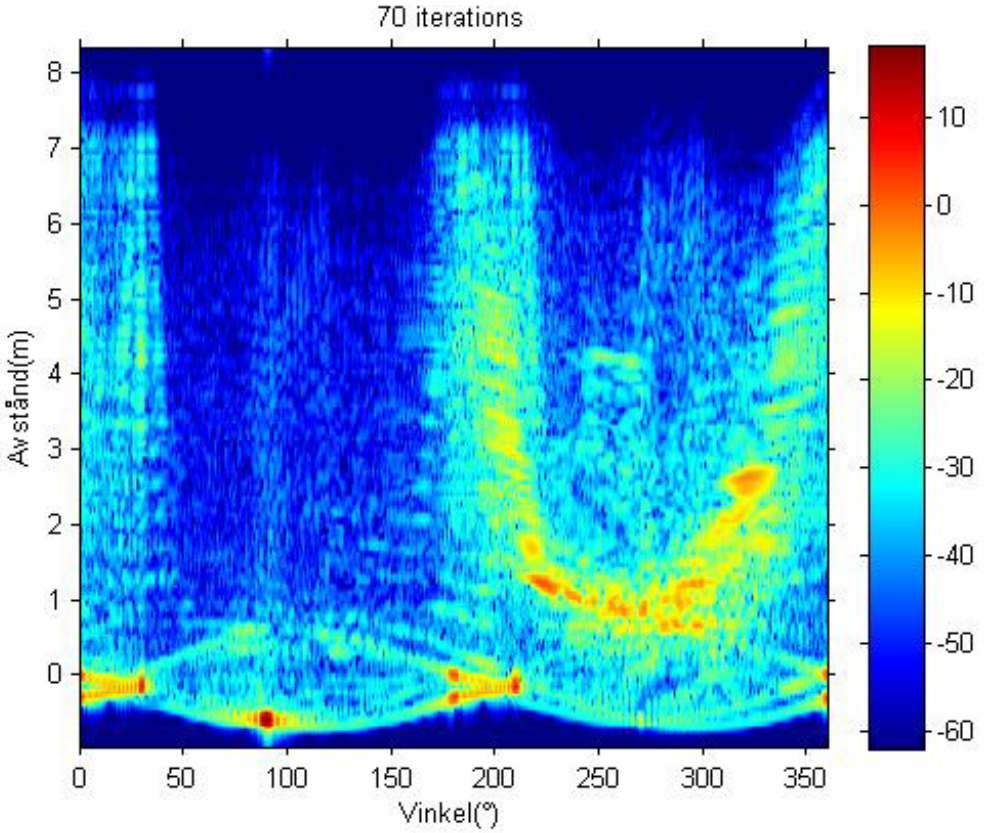

Figure16. Range profiles from calculated data. Intensity scale in dB *(see footnote 2).*

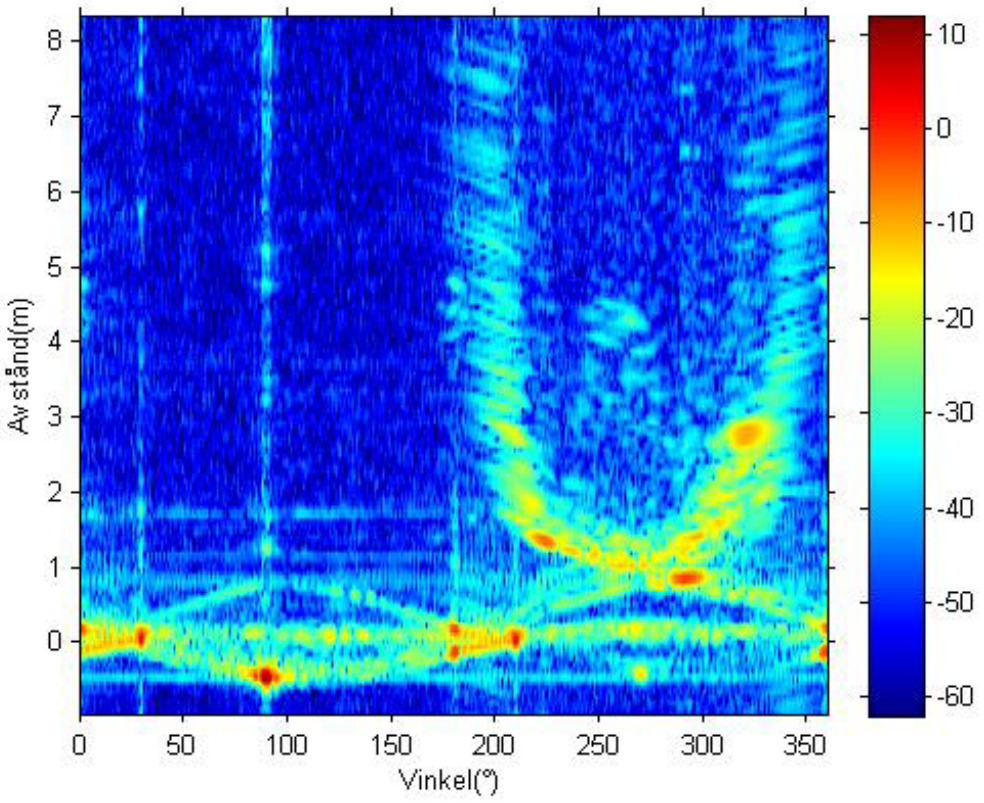

Figure 17. Range profiles from measured data. Intensity scale in dB *(see footnote 2).*

Turning to figures 14-17 and neglecting the support and the intensity scale adjustment, the agreement between calculated and measured data appears to be good to excellent despite the complex nature of the target object. If there are any errors resulting from the use of facets that are too large in relation to the wavelength they are at least not very conspicuous. As known from measured profiles in figure 10 the tails from multipath scattering in the cavity do persist weakly beyond the present unambiguity range, but the calculated tails stop just short of it. If the range profiles in appendix A are studied it seems likely that the tails would grow longer if the calculations would be continued past 70 iterations, but the effects on the RCSs in the frequency domain are likely to be small.

The calculations can be seen to reproduce individual features like the intensity spot near 320º 2.6 m and the short weak band from 245 to 270º at 4.2 m. On the other hand the prominent spot near 290º 0.8 m is considerably less prominent in the calculated result. ISAR images (appendix B) suggest that it is related to returns from the cavity bottom. At 210º the multipath tail appears to be reproduced out to at least 5 m behind the aperture of the cavity.

In a GO picture this would correspond to $2 \cdot 5 \cdot \left|\cos 210°\right| / 0.3 \approx 29$ bounces in a straight cavity with a 0.3 m inner diameter. On the other hand such a cavity would be $5 \cdot \left|\sin 210°\right| \approx 2.5$ m deep making such a comparison questionable. The stronger patches of intensity on the more proximal "bent" parts of the multipath tails could be better candidates for a GO interpretation. Both tails qualitatively follow a pattern that would be expected for GO bouncing to the bottom of a straight cavity. The existence of an asymmetry between the left and right branch is not unexpected since the cavity is not symmetrical with respect to the 270º direction. However, the effective depth of the cavity seems shorter for the left branch which is surprising since directions in the right branch point more in the average direction of the cavity.

In the backside range 0 to 180º, where the cavity aperture is not seen by the radar, the calculated range profiles are very clean in front of the cavity while at the back there is, unexpectedly, significant intensity. This will be referred to as calculation hum[3]. In the measured data there is noise reaching similar levels both in front of and behind the cavity, but the level is similar on both sides. If there were a true RCS component similar to the calculation hum, the noise would be likely to hide it partly, but not fully, since the hum and the noise appear to be of similar strengths. A tentative hypothesis is that the calculation hum is caused by incomplete cancellation of the contributions from hidden currents. The intensity leaking from strong RCS sources, e.g. cylinder broadsides, is much more pronounced in the measured profiles than in the calculated indicating leakage e.g. through phase noise.

4.2 ISAR images

Simulated ISAR (inverse synthetic aperture radar) images for the calculated data were generated using the full 7.992 to 10.008 GHz range giving a resolution of 75 mm. An angular sector of total width13.2º around each centre angle was used to give a matching crossrange resolution. The ISAR map area is a square with 9.3 m edge length based on the downrange unambiguity distance. As previously mentioned the crossrange unambiguity is only 2.4 m so there will be several ambiguous, defocused, images to the left and to the right of the properly focused central object image. Due to the rather large area imaged the images were calculated without oversampling. No filter (such as Hanning), but "rectangular" data, was used in the image generation.

[3] Noise is stochastic while disturbance signals picked up from external sources is classically referred to as hum. Since we suspect that this is non-stochastic calculation errors we prefer to refer to it as hum.

For the measured data the same area is imaged but the full 8 to 12 GHz range is used with a 23.25º sector width giving a resolution of 38 mm. The resolution and the frequency range are thus somewhat different from the calculated data, but priority was given to displaying the best resolution available. The same ISAR map area was used as for images based on calculated data. The unambiguity ranges are large enough to make ambiguous overlap rather insignificant (cf. figure 10).

The prime area of interest is, of course, the cavity region, nominally 180 to 360º. A few sample images will be shown in this section, but otherwise the reader is referred to the appendix where images for every 10º in this region can be found. The open end of the cavity is facing downward and the direction from the origin towards the radar is marked by a white dot. The object is symbolised with a white line overlay. For angles and object section designations A-E please also refer to figures 3 and 6.

ISAR images for measured data are displayed using the default automatic intensity scale. Differences in the two datasets lead to differences in the ISAR processing gain, cf. footnote 2, which together with the suspected shortcomings of the measured intensities [section 4.1] make a quantitative comparison of ISAR intensities difficult. The intensity scale of the images based on calculated data has therefore been set to the same 50 dB span as those for calculated data and the upper scale limit was set to a value that empirically enhances the similarities between the two sets of images.

Even with perfectly calibrated data and a formal analytical treatment of the processing gain, the differences in bandwidth and frequency step etc. would lead to differences, which should be kept in mind. The measured images have higher resolution, but, since the angular sector used for their generation is larger, strong specular reflexes will be seen over a larger range of centre angles. Radar returns that are not properly focused, e.g. multipath contributions, will often smear in the angular direction over a range corresponding to the sector width, making the two sets of images differ.

The measured data also includes target support contributions which are often prominent near the centre of the images. Furthermore the lid makes the physical target different from the CAD model, and careful measurements in the range profiles do show that it is somewhat longer than 1.2 m due to the thickness of the lid. The ISAR images show larger differences than the range profiles but this is largely due to the differences in ISAR generation and in general the agreement is still good.

The strong reflexes of the cylindrical sections are, as expected, seen over a wider range in the measured data where a larger ISAR sector has been used (seen e.g. at 220º figure 22-23 and appendix). Also expected is that support structures often show up near the image centre for the measured data (seen e.g. at 220, 260 and 310º figures 22-23, 18 and appendix).

The cavity rim shows up clearly at 270º (appendix only). It is not strong, but on the other hand it is unrealistically thin in this generic model.

In the range profiles most of the multipath intensity appear in the two curved intensity tails that start near the cavity bottom at 270º and then accelerate toward larger distances as the angle increases or decreases. As previously discussed these correspond to complex scattering in the cavity.

In the ISAR images the tail appears in an extended region downrange from the cavity aperture. It does not seem to provide much crossrange information other than the crossrange position of the aperture. Even though it appears outside the object the direction to the object is correct and a radar seeker would steer towards the intake.

As seen already in the range profiles the cavity does not seem to be a significant scattering source at angles near 180 and 360º degrees because the projected aperture area is then small, and diffraction at the cavity edge does not seem to contribute anything to the monostatic return. As the radar angle becomes less glancing with respect to the aperture plane the multipath tail appears, but is at first weak and diffuse. The onset of the tail is getting distinct

and dominant at 220º. The prominence of the onset of the tail persists until 300 or 310º (figure 19), i.e. on this side of 270º this characteristic behaviour cover a somewhat smaller angular range. The tail intensity remains rather significant to 330º corresponding to the prominent range profile spot centred at 320º 2.6 m (figures 16-17), and then gradually loses intensity.

It may be tempting to assign the tail onset to returns from a beam bouncing into the cavity and back out. This hypothesis might be tested by comparing their positions with estimates of the corresponding GO ray path. Due to the cavity bends this requires ray tracing, which cannot be included in this study. Preliminary tests have indicated positions deviating significantly from analytical position estimates for straight cavities. The range profile (ISAR) distance appears to be too short at angles below 270º and too long at higher angles despite the fact that some optical sight to the bottom is expected in the 270 to 297º range. This can be seen in the ISAR images, but perhaps better in the range profiles, figures 16-17. In the absence of ray-traced estimates for the curved cavity and considering this contra-intuitive trend of the tail onset no such assignments are made.

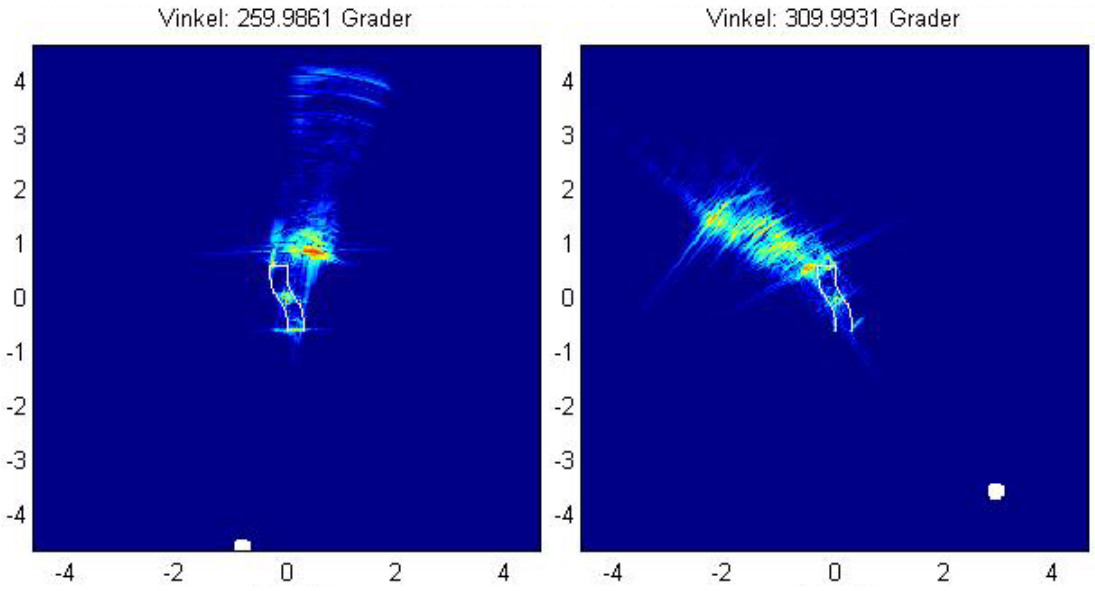

Figures 18-19. ISAR images with centre angles 260 and 310º for measured data. Note the support structures near the origin and the aperture rim visible for 260º. The tail structure for 260º starts with a pronounced bottom return and ends with the 4.2 m *feature.*

The second strongest feature of the range profiles, having much less intensity, is found around 245 to 270º at a range of 4.2 m (figures 16-17). In the ISAR images this only shows up as rather marked end to the tail (figure 18 and appendix). There are few if any distinct range profile features apart from these although there are certainly weak patches of intensity here and there that can be expected to contribute with tailing at the corresponding range and angle in the ISAR images.

At 230º (figure 20-21) the onset and at 330º (appendix B) the tail is split in two spots in contrast to the calculated data. At 270º (appendix B) the strongest experimental hotspot is not found behind the aperture but slightly to the right. This is probably due to strong returns near 260º (figure 18 and appendix B) contributing to this image. The calculated image also tends to this behaviour but its ISAR sector is more narrow. At 310º the multipath tail for measured data appears slightly bent.

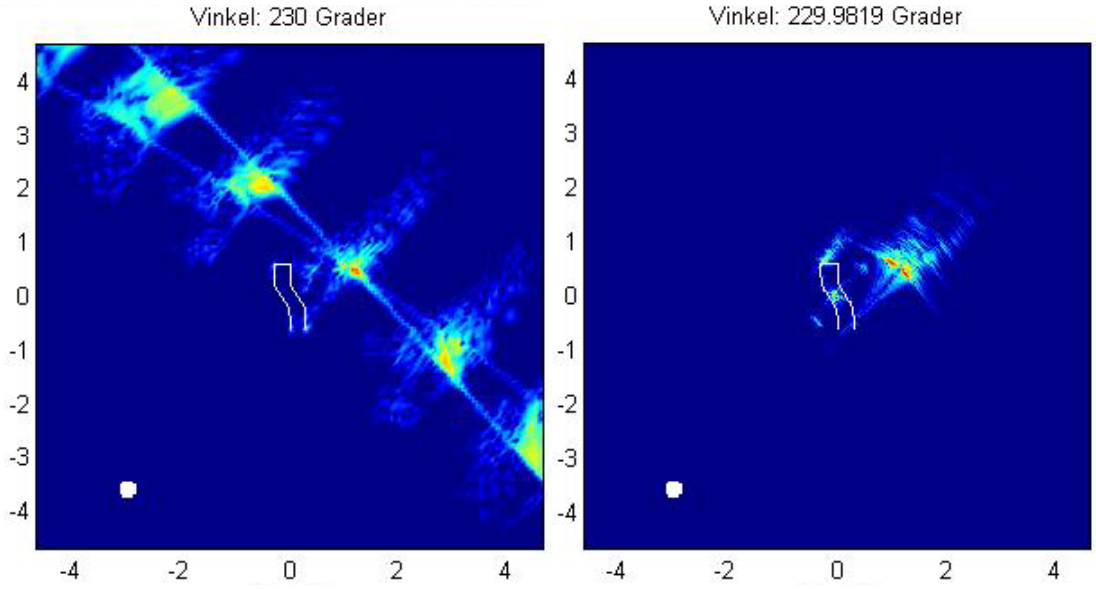

Figure 20-21. ISAR images at 230º for calculated (left) and measured (right) data.

The calculated data on the other hand shows additional tails at 210º (appendix B only) to 220º (figures 22-23). The calculated data also shows tailing at 0º (appendix B, 360º), 30º (figures 24-25) and 180º (appendix B) degrees where the experimental data show no or only very weak tailing. It is likely that this is related to the tentative calculation hum discussed for the range profiles.

There is also a tendency for the calculated data to show some weak diffuse intensity, tracing the object in cases where the measured object images appear quite different. This can be seen e.g. at 220º (compare figures 22-23), 310º and 320º (see appendix B for comparisons in the latter two cases), and is likely to be true images deriving their intensity from weak sidelobes while the images based on measured data and a larger ISAR sector may have contributions

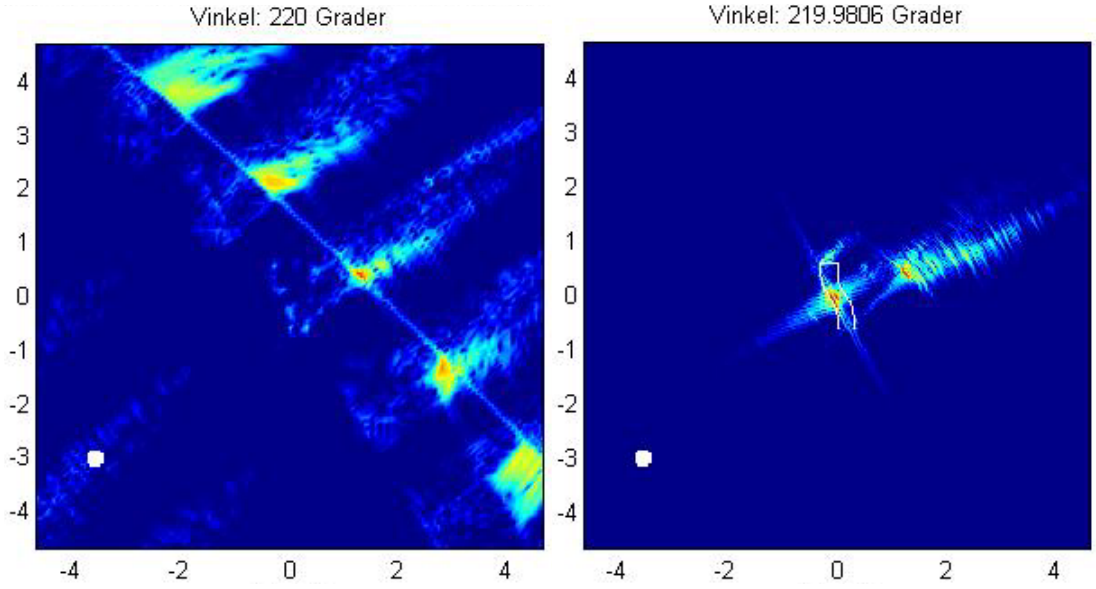

Figures 22-23. ISAR images for calculated and measured data at 220º. Note the additional, upper, tail seen in the calculated (left) image. The strong difference in object body intensity is due to a difference in ISAR sector width. The overlay is not included in the left image to allow a more detailed study of this region. In the right image the support cylinder (figure 7) may be seen on the inside of the strong C section (figure 3) return.

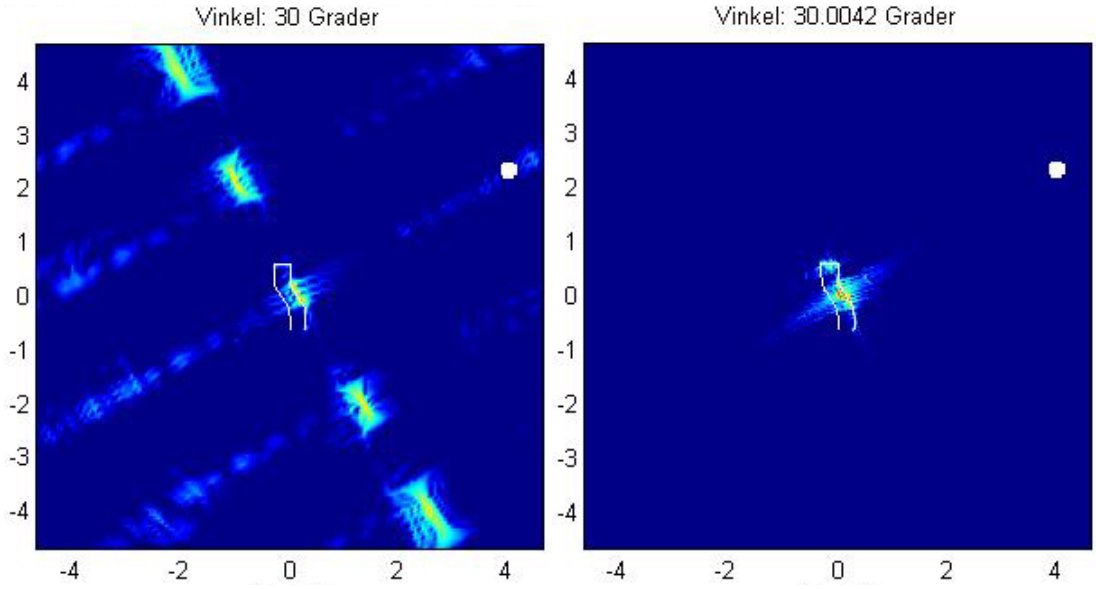

Figures 24-25. ISAR images for calculated and measured data at 30º. Note the pronounced tailing for calculated data which could be due to cancellation errors.

from stronger sidelobes. The 220º case (figures 22-23) is a striking example of how the difference in ISAR sector can make the images appear very different. The image generated from measured data with a wider sector includes considerable intensity from the C section (figure 3) peaking at 210º (see e.g. figures 16-17).

In the 0 to 180º range signature of the cavity is mostly rather low since there is nominally no illumination of the aperture. Cylindrical sections and the outer cavity bottom give strong returns at 0, 30, 90 and 180º and the bends give returns of intermediate strength in the 0 to 30º range. In addition to this support returns are seen in most experimental images. One peculiar difference is that while in the measured data (figure 27) the A and E sections (figure 3), as expected, give straight uninterrupted line spots corresponding to their length at 0/180º these spots are partly interrupted in the calculated data (figure 26).

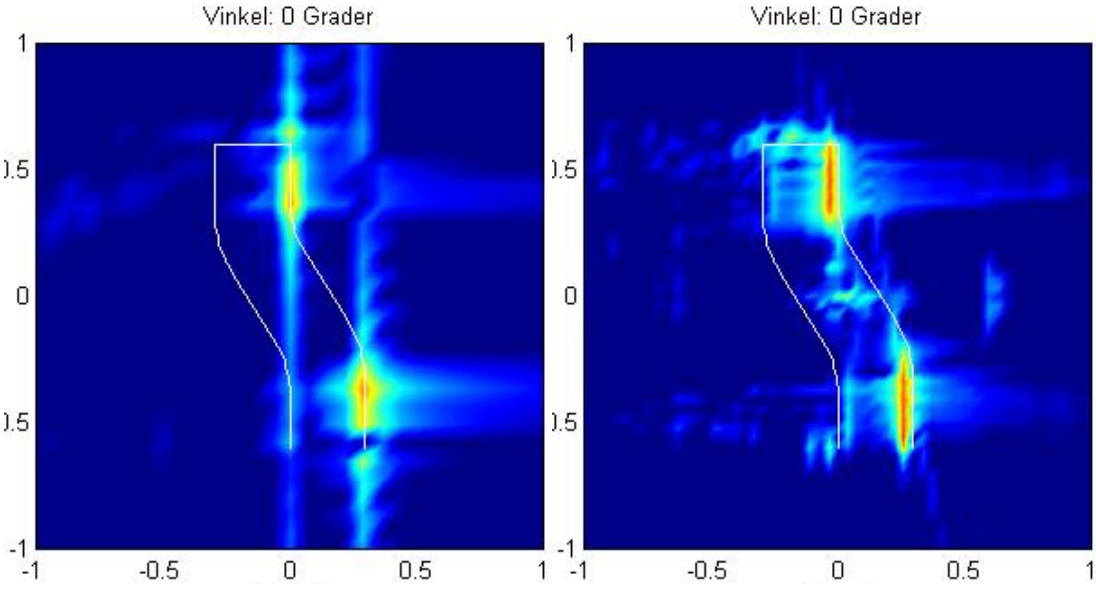

Figures 26-27. Details displaying the differences in calculated (left) and measured (right) A,E cylinder section reflexes.

5 Conclusions and outlooks

The validity of the IPO method for complex radar targets of intermediate size appears to have been confirmed. In this study clear cases of divergence have only been found when pushing the frequency beyond accepted limits. However, other settings, e.g. the use of high relaxation parameter values (α_{rel} approaching 1) may lead to less stable convergence.

As pointed out by others [5] and as discussed in the introduction (Sec. 2) the method compares very favourably with MoM (method of moments) with respect to object size, frequency and calculation speed. However the result cannot be expected to be as accurate as for MoM.

IPO could probably, with advantage, be applied to electromagnetic calculations other than RCS. While MoM in many cases may be preferred for antennas problems like large reflector antennas or antennas together with surrounding structures may be examples of such problems.

It appears that IPO is sometimes able to produce excellent results even if some facets of the CAD model are too large or even if the model is not closed. However, until the conditions required for this have been established it should be avoided.

When too high frequencies have been tested, this has typically resulted in too high RCS values. This suggests that IPO results could be used as conservative estimates even if it has not been established that the frequency is low enough for the CAD model used. However, this would need theoretical or solid empirical support.

There are many aspects of IPO calculations that deserve further study e.g. convergence, causes for and detection of divergence, accuracy and the nature of the approximations made, the use of apertures, the effects of different shadowing criteria, and application to other benchmark problems. The code could be improved by adding convergence testing, non-PEC surfaces and a better user interface.

It is necessary to have access to a versatile CAD tool in order to efficiently prepare CAD models not having larger facets than permissible while keeping the number of facets as low as possible in order to conserve memory and keep the calculation times down. The Rhinoceros CAD tool does not really provide sufficient control over faceting for this.

The IPO method as such does not limit the size of problems that can be treated. The size of the problem may be expressed in the number of facets required which depends on the frequency and the object size. In practice the problem size will be limited by calculation time, and, in matrix-based implementations by the memory available. The time required can be expected to increase with the fourth power of the product of frequency and linear object size[4], and the same will hold for memory in matrix-based algorithms.

Presently memory limitations and costs make the use of secondary memory potentially attractive if the severity of the speed penalty for memory swapping can be overcome. Solid state drives (SSD) offer the prospect of faster secondary memories but may still be somewhat immature and the OS support for memory management is not likely to be efficient enough requiring special solutions.

Future computers will have more memory, and memory could be saved by using sparse matrices, data compression etc, but the permissible frequency (or object size) increases slowly with the amount of available memory. Efficient methods for filling the coupling coefficients (i.e. the matrix elements) would reduce the speed penalty for memory-lean solutions and memory-lean solutions (not filling complete matrices but recalculating the coefficients) may perhaps gain more from convergence testing. The use of compiled code,

[4] Or, to be more accurate, with the fourth power of frequency and the second power of object surface area.

e.g. Fortran or C, is likely to provide for better memory management, faster speed and could be better for memory-lean algorithms and more aggressive convergence testing.

If, hypothetically, the facet size could be increased beyond λ/2 the f^4-problem would remain, but the onset of severe problems would be moved to higher frequencies or larger object. If the facet size could be increased from λ/3-λ/2 to just λ this would correspond to an increase in memory capacity of between 16 and 81 and even if coefficients for larger facets will be more complex to evaluate the number of evaluations will be similarly fewer making an overall increase in calculation speed. The permissible frequency, or linear object size, is thus likely to grow approximately in proportion to the permissible facet size.

It is far from evident that the facet size can be increased since it seems to be related to the sampling theorem. However, if not only the surface current density is sampled, but the phase gradient across the facet also is known it may be possible to find analytic coefficients for larger facets. After all there are indeed PO expressions, the Mitra-Lee formula for the bistatic scattering from arbitrarily large polygons, where the phase gradient is given by the combination of the wave vectors of the incident and the scattered waves, $\bar{k}_{inc}$ and $\bar{k}_{scat}$.

Polygons in IPO CAD models could hardly be arbitrarily sized since the expressions assume far-field conditions and constant illumination across the surface, and furthermore many object surfaces are not flat. As just demonstrated even modest increases in the permissible facet size would be very valuable.

6 References

[1] B. G. Smith, “Geometrical Shadowing of a Random Rough Surface” *IEEE Trans. on Antennas and Propagation*, vol. 15, 668-671, 1967.

[2] M. I. Sancer, “Shadow-Corrected Electromagnetic Scattering from randomly Rough Surface” *IEEE Trans. on Antennas and Propagation*, vol 17, pp. 577-585, 1969

[3] Fernando Obelleiro-Basteiro, Jose Luis Rodriguez and Robert J. Burkholder, “An Iterative Physical Optics Approach for Analyzing the Electromagnetic Scattering by Large Open-Ended Cavities”, *IEEE Trans. Antennas and Propagation,* Vol. 43, No. 4, 356-361, April 1995.

[4] Robert J. Burkholder, “A Fast and Rapidly Convergent Iterative Physical Optics Algorithm for Computing the RCS of Open-Ended Cavities”, *ACES Journal*, Vol. 16, No. 1, March 2001.

[5] R.J. Burkholder and T. Lundin, “Forward-backward iterative physical optics algorithm for computing the RCS of open-ended cavities”, IEEE Trans. Antennas Propag. 53, 793-799, 2005.

[6] Jonas Rahm, Magnus Gustafsson, Magnus Herberthson, Erik Zdansky, Stefan Nilsson, Anders Örbom, ” Comparison between measured and calculated bistatic RCS data on a rough metallic background surface”, FOI-R--3102—SE, Linköping 2010.

[7] Jonas Rahm, Magnus Gustafsson, ” Iterativ fysikalisk optik (IPO)”, FOI-R--2416—SE, Linköping 2008.

[8] Rolf Persson och Roland Lindell, ”IR measurements on S-ducts”, FOI Memo H0533, Juli 2008.

[9] S. Nilsson, M. Wilow, N. Karlsson och A. Örbom, "Improvements of the Swedish outdoor RCS measurement capability", *AMTA Europe Symposium*, München, 1-4 maj 2006, Conference proceedings 118-123.

[10] J.Rasmusson, N. Gustafsson och J. Rahm, "Outdoor broadband RCS measurements of model-scale aircraft", *AMTA*, Cleveland USA, 3-8 november 2002 Conference proceedings 439-444 (FOI-S--0698-SE).

[11] E.F. Knott, J.F. Schaeffer, M.T. Tuley, "Radar cross section" 2:nd ed. Artech House (1993), ISBN 0-89006-618-3.

Appendix A: The development of RCS and range profiles during iteration

Convergence as followed through RCS(φ,f) [dBm^2] and downrange profiles. The results from the final iteration are compared with a subset of measured data consisting of nearly the same frequencies (7.992 GHz missing) but a denser angular sampling (7200 angles/360º turn instead of 900). ISAR images from these data are shown in the text and in the next appendix. Footnote 2 deals with the intensity scale of the range profiles.

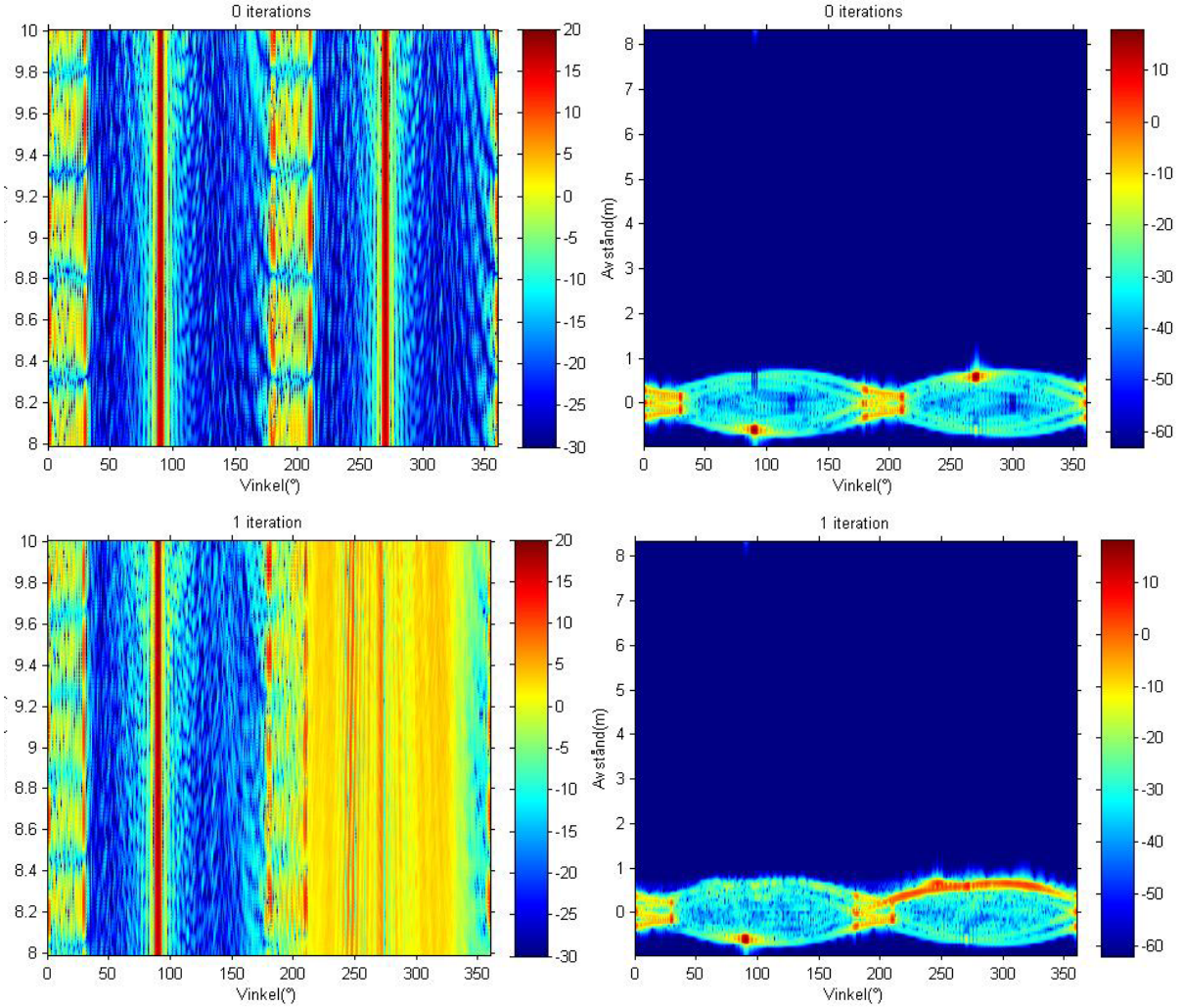

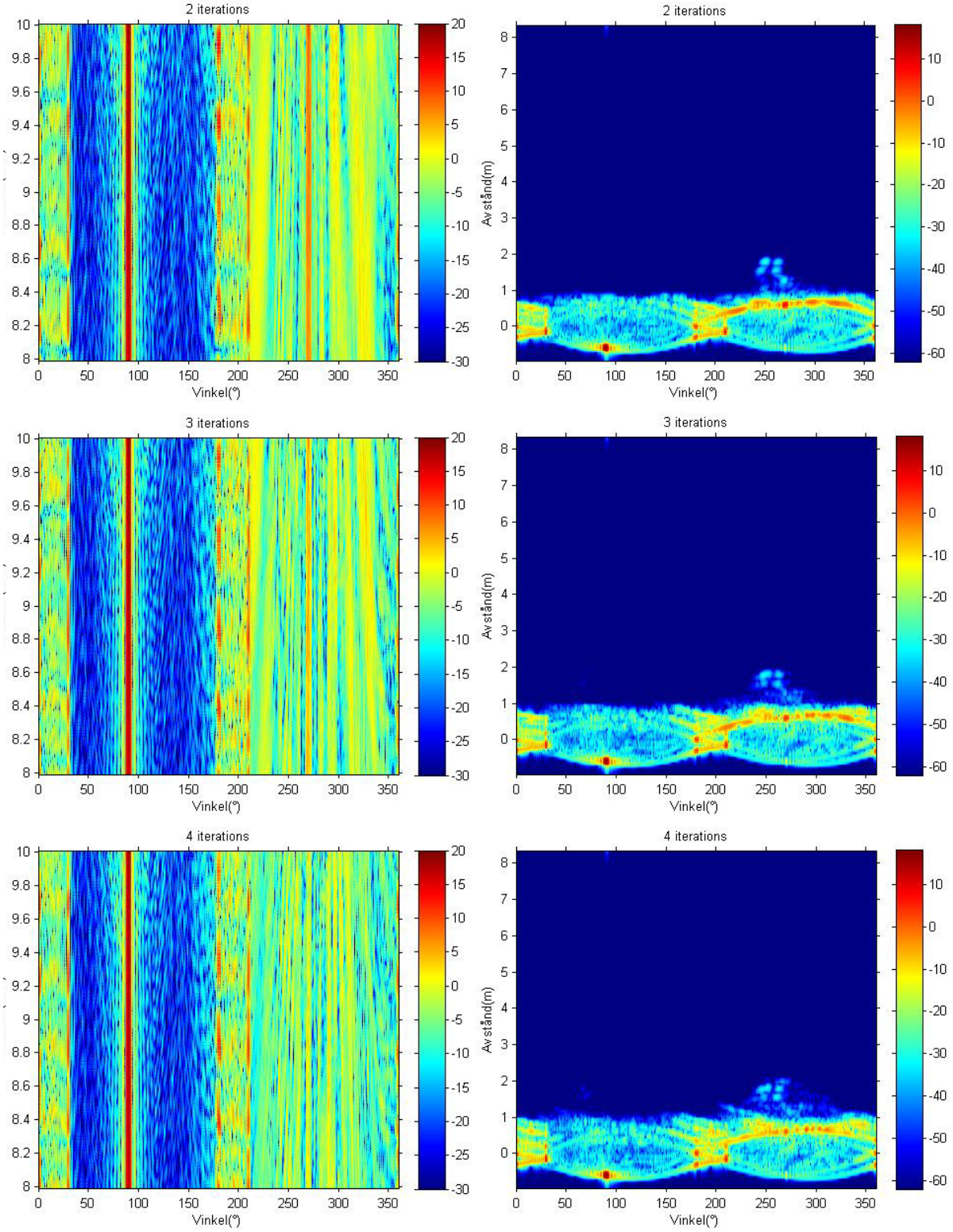
2 iterations
Vinkel(°)
2 iterations
Avstånd(m)
Vinkel(°)
3 iterations
Vinkel(°)
3 iterations
Avstånd(m)
Vinkel(°)
4 iterations
Vinkel(°)
4 iterations
Avstånd(m)
Vinkel(°)

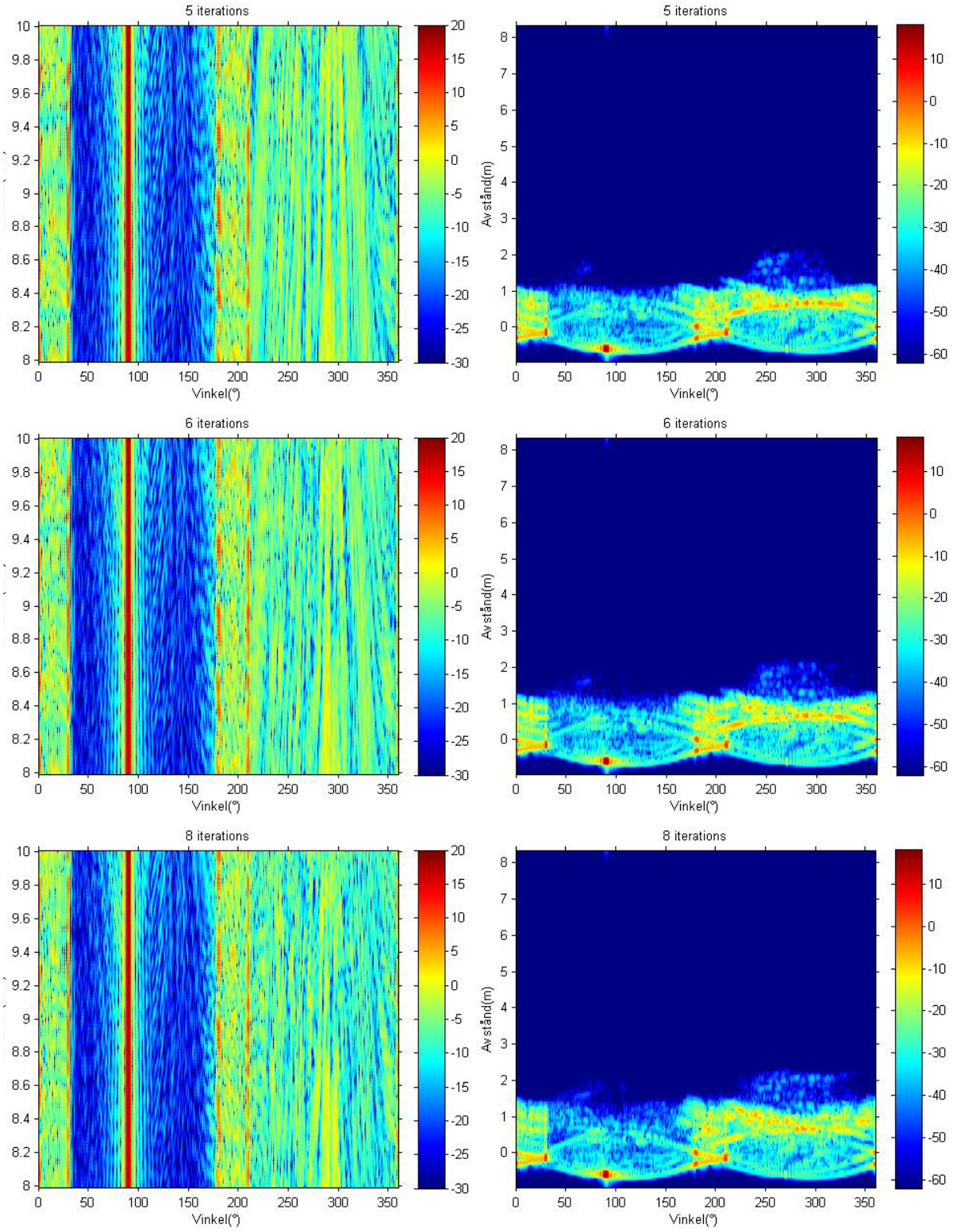
5 iterations
Vinkel(°)
5 iterations
Avstånd(m)
Vinkel(°)
6 iterations
Vinkel(°)
6 iterations
Avstånd(m)
Vinkel(°)
8 iterations
Vinkel(°)
8 iterations
Avstånd(m)
Vinkel(°)

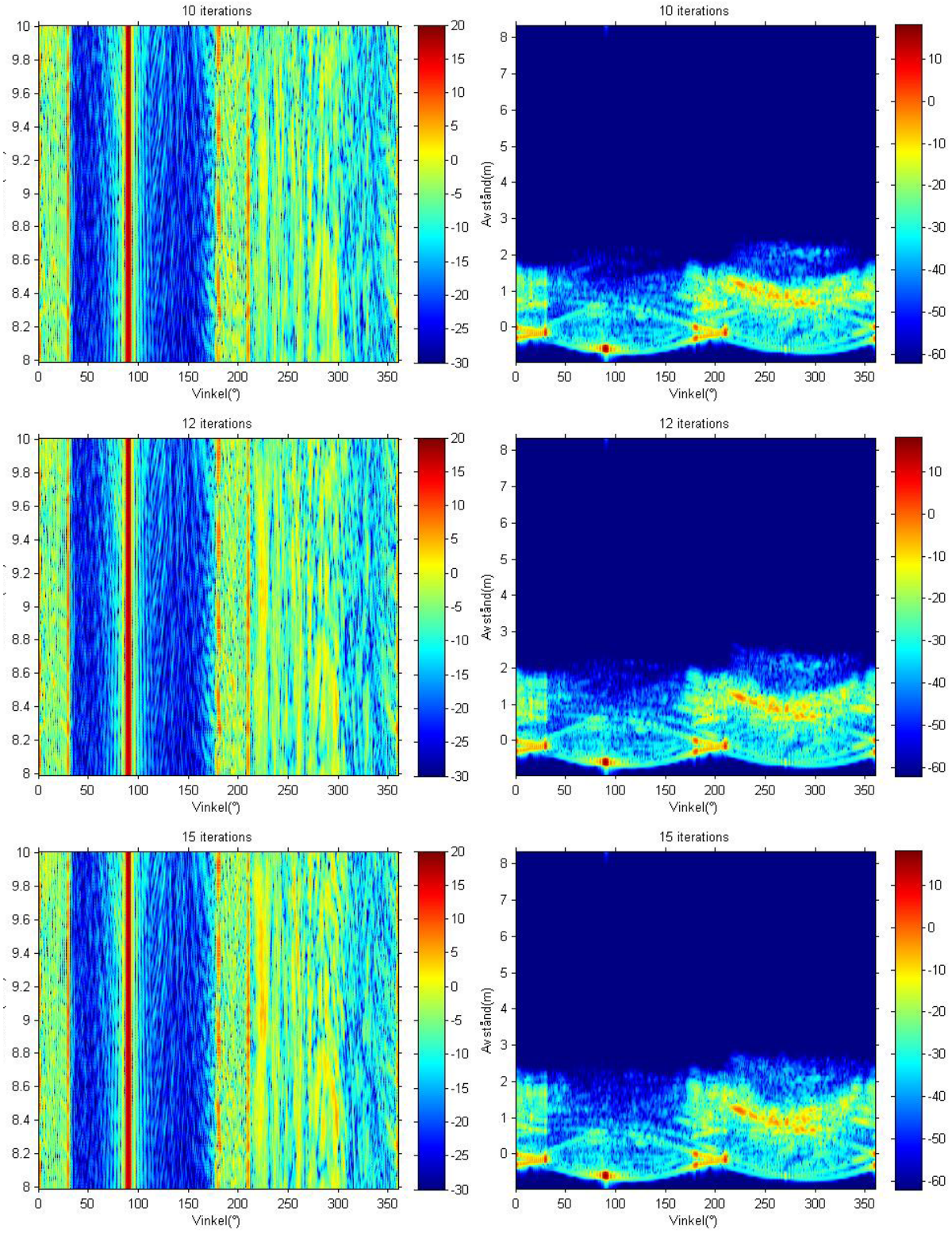
10 iterations
Vinkel(°)
10 iterations
Avstånd(m)
Vinkel(°)
12 iterations
Vinkel(°)
12 iterations
Avstånd(m)
Vinkel(°)
15 iterations
Vinkel(°)
15 iterations
Avstånd(m)
Vinkel(°)

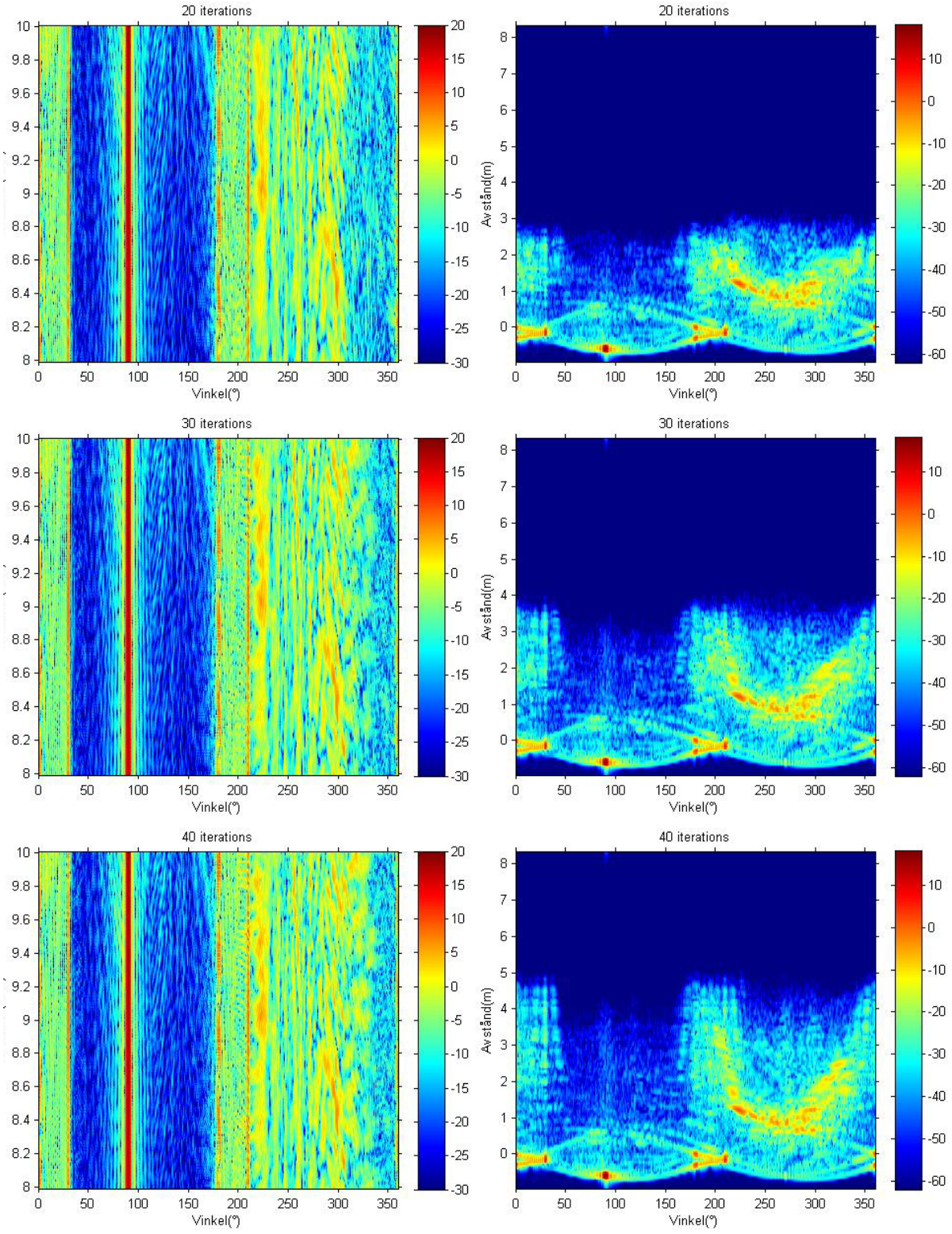
20 iterations
Vinkel(°)
20 iterations
Avstånd(m)
Vinkel(°)
30 iterations
Vinkel(°)
30 iterations
Avstånd(m)
Vinkel(°)
40 iterations
Vinkel(°)
40 iterations
Avstånd(m)
Vinkel(°)

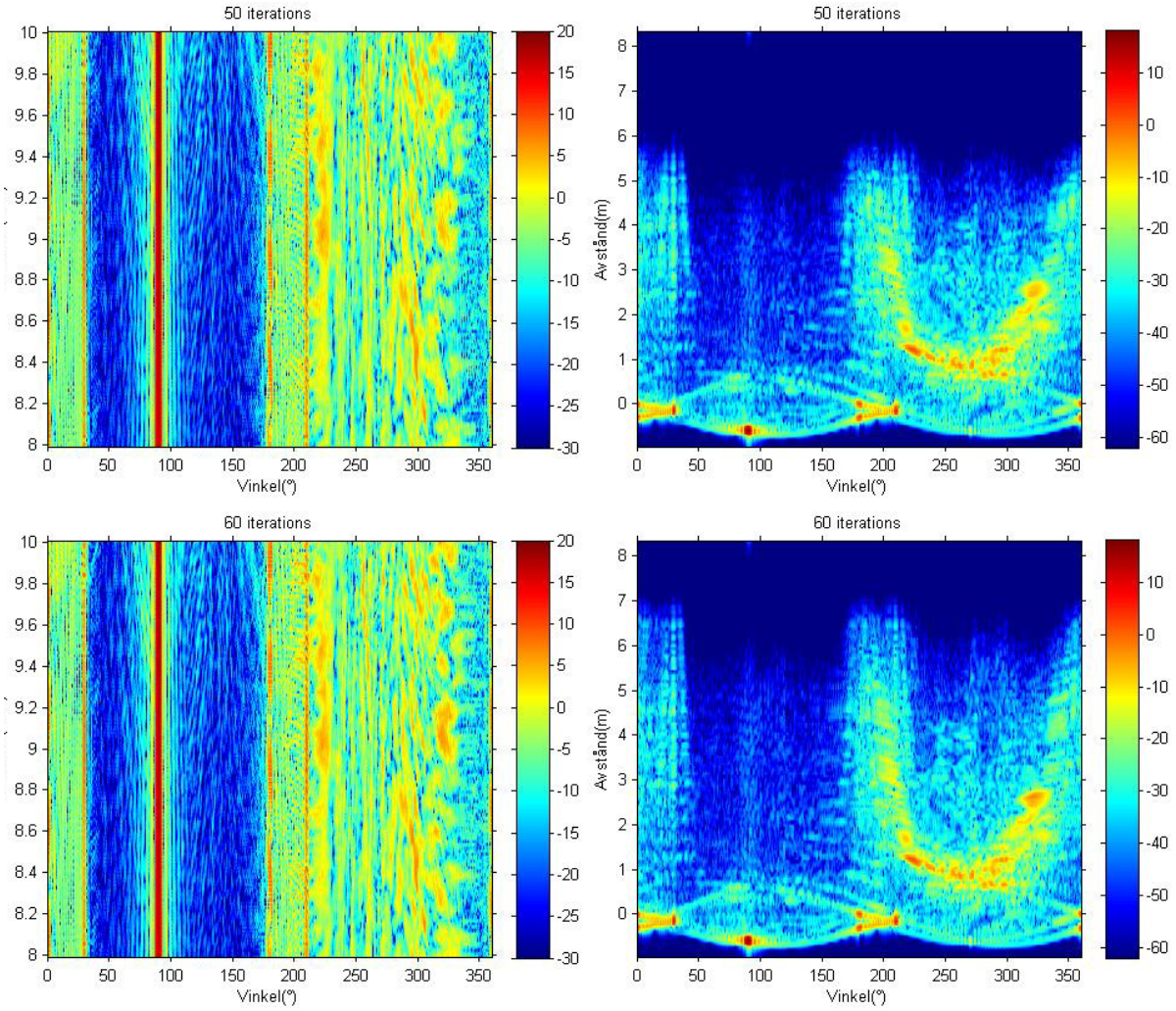
50 iterations
Vinkel(°)
50 iterations
Avstånd(m)
Vinkel(°)
60 iterations
Vinkel(°)
60 iterations
Avstånd(m)
Vinkel(°)

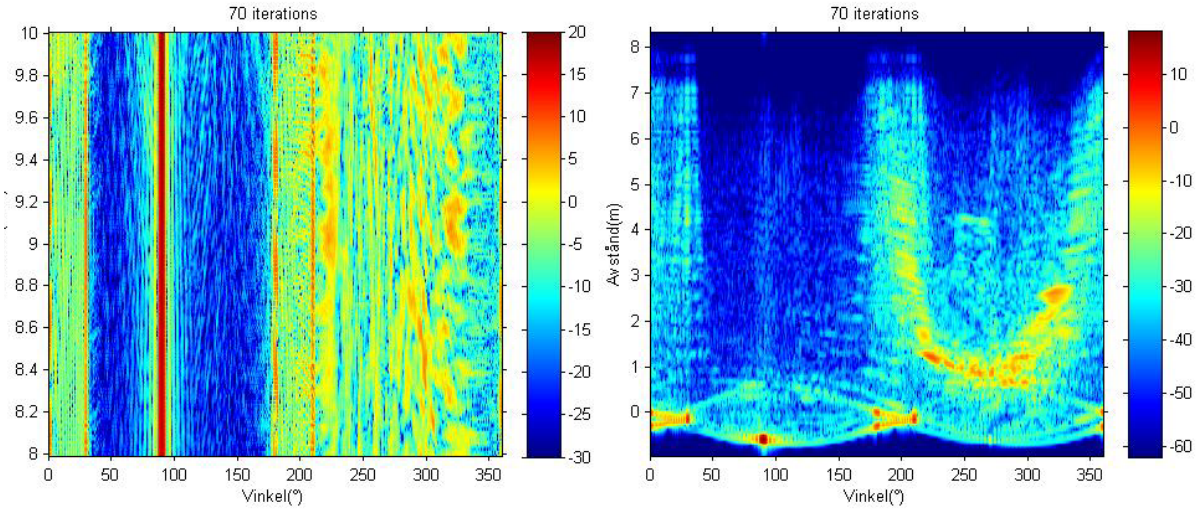

Calculated results after 70 iterations.

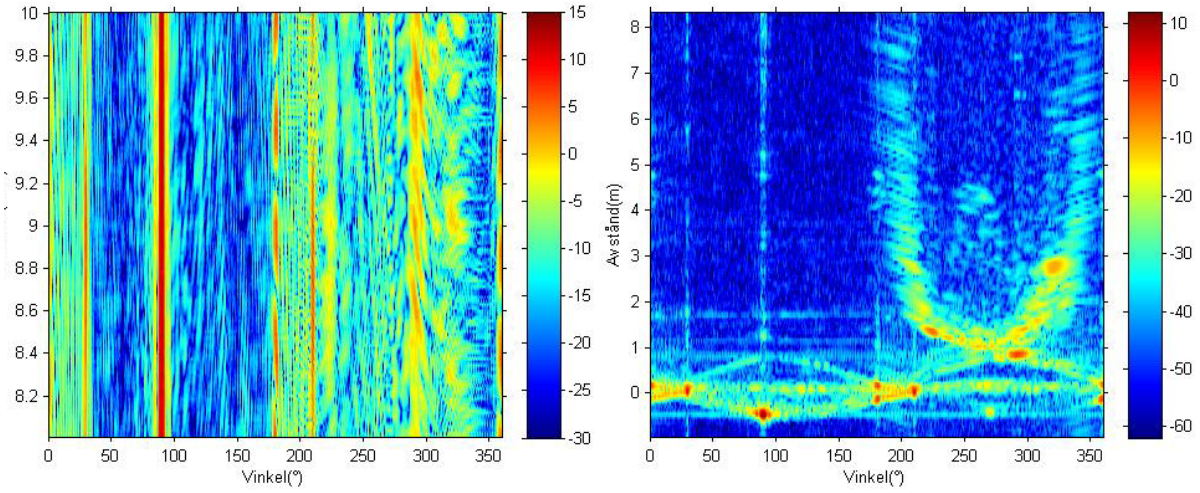

Measured results.

Appendix B: ISAR images of the cavity for calculated and measured data

ISAR images are here shown for every 10º in the angular range 180 to 360º i.e. the range where the radar nominally illuminates the cavity aperture. The images are based on IPO calculations (left) and measurements (right). As explained in section 4.1 the intensity scale span is the same for all images and the intensity range of the calculated images has been adjusted to be roughly comparable to the images based on measured data. The intensity scale units are treated in footnote 2. The calculated images have a short unambiguity distance in the crossrange direction, but large enough to keep overlap problems small. The full bandwidth has been used in both sets in order not to sacrifice resolution. Due to its larger bandwidth a wider ISAR sector has been used for the measured data. These differences, together with measurement support and the cavity lid, are the main sources of differences between the two sets of images. The open end of the cavity is facing downward and the direction from the origin towards the radar is marked by a white dot. The object is symbolised with a white line overlay.

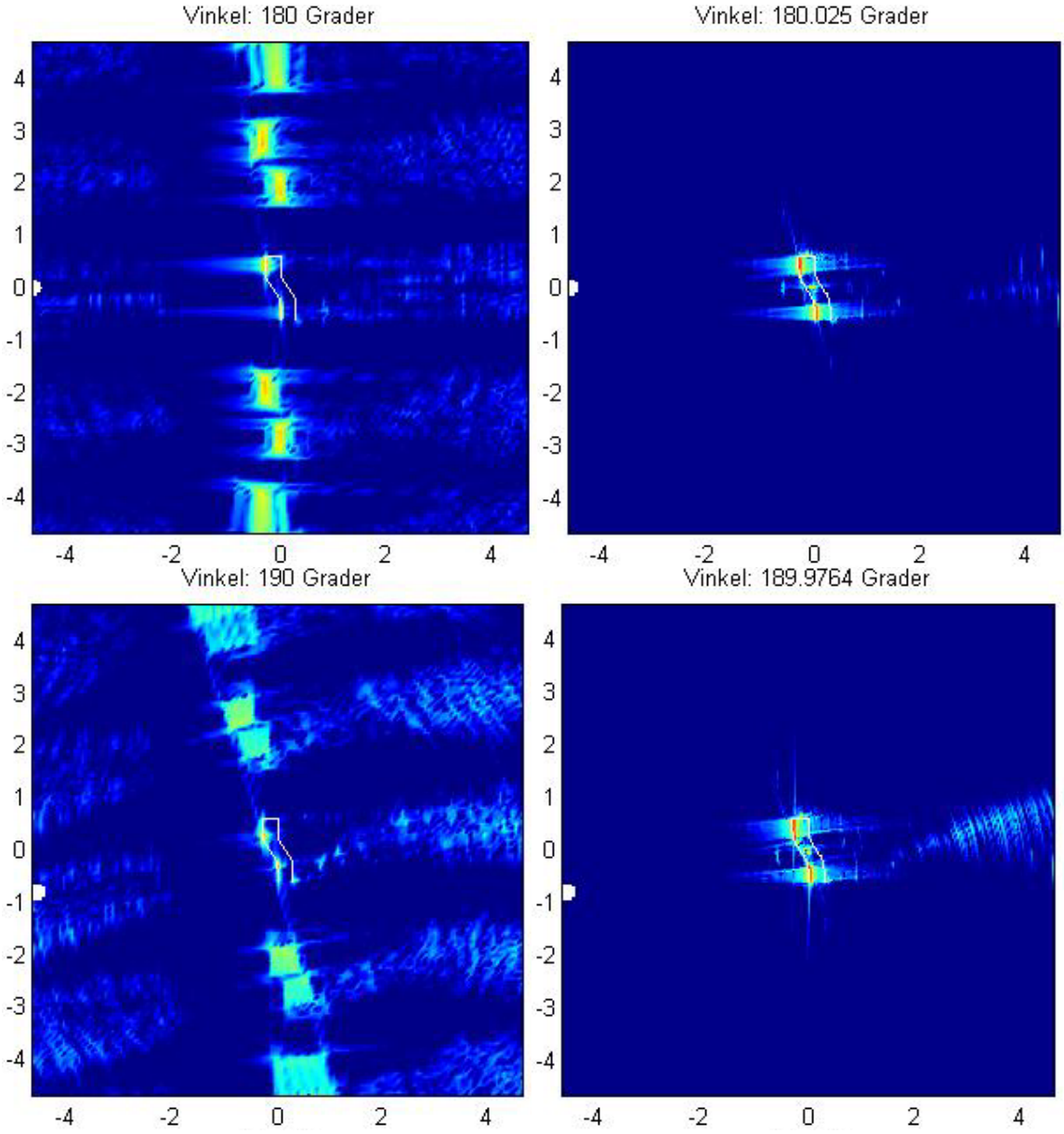

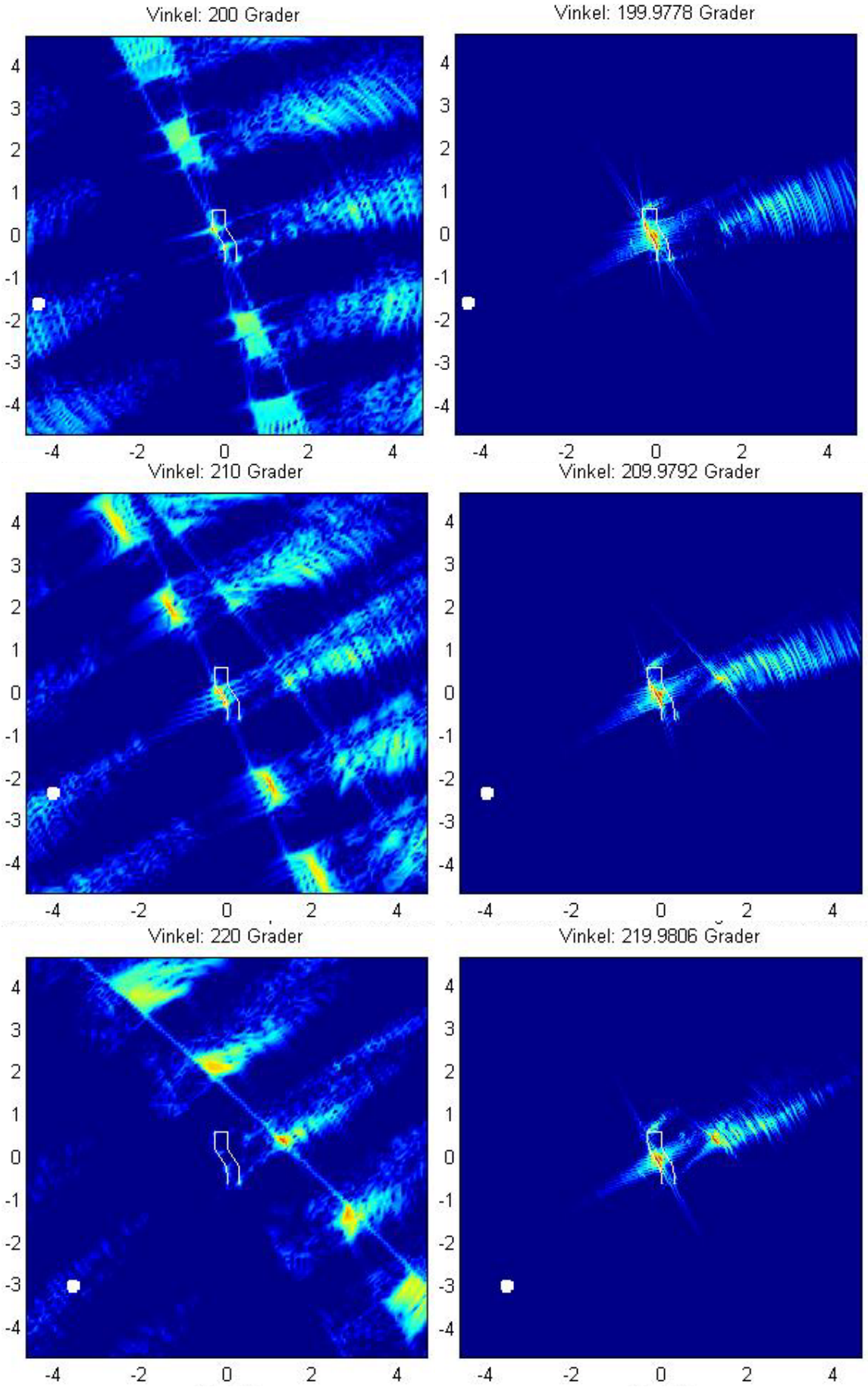
Vinkel: 200 Grader
Vinkel: 199.9778 Grader
Vinkel: 210 Grader
Vinkel: 209.9792 Grader
Vinkel: 220 Grader
Vinkel: 219.9806 Grader

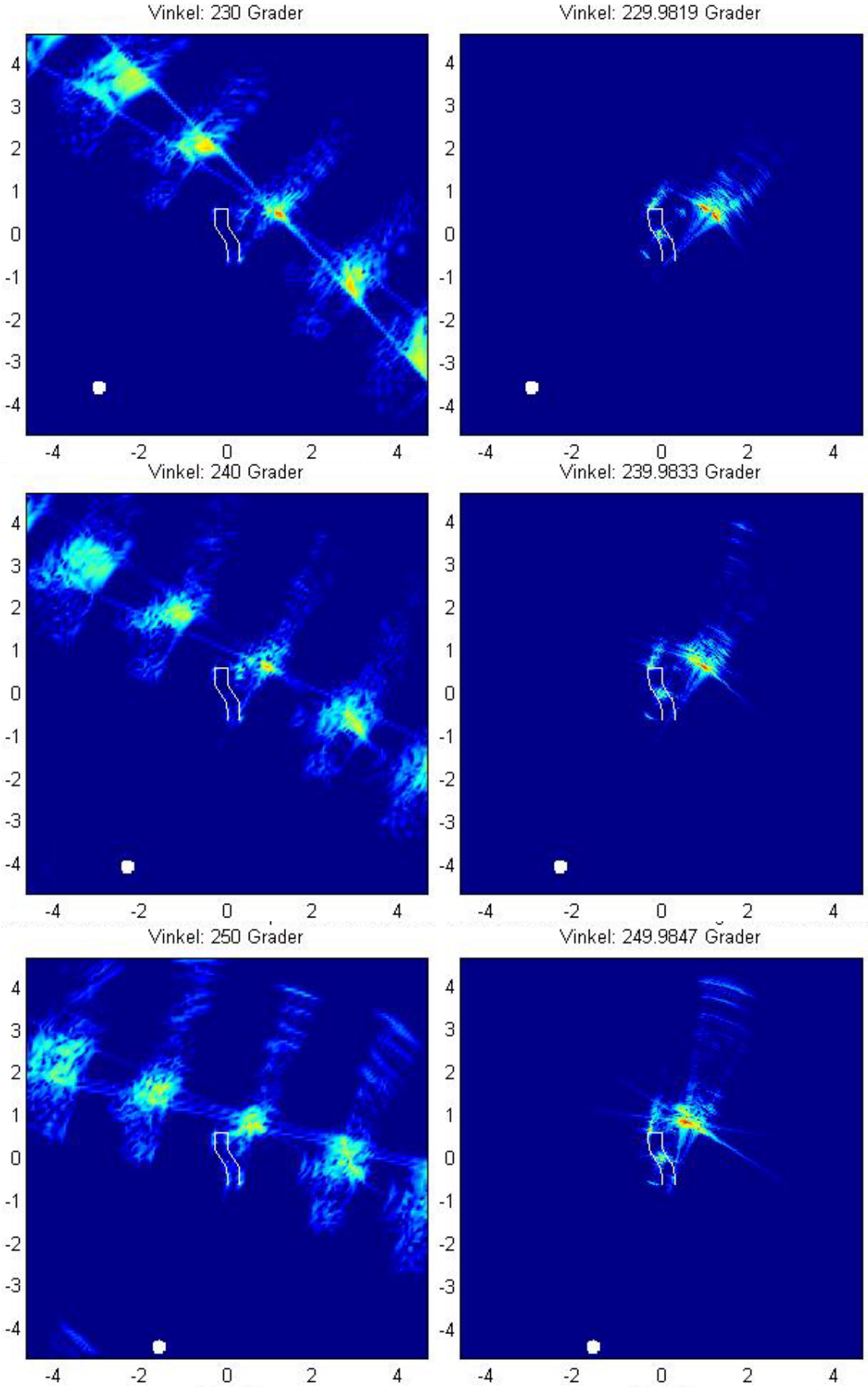
Vinkel: 230 Grader
Vinkel: 229.9819 Grader
Vinkel: 240 Grader
Vinkel: 239.9833 Grader
Vinkel: 250 Grader
Vinkel: 249.9847 Grader
4
3
2
1
0
-1
-2
-3
-4
-4
-2
0
2
4

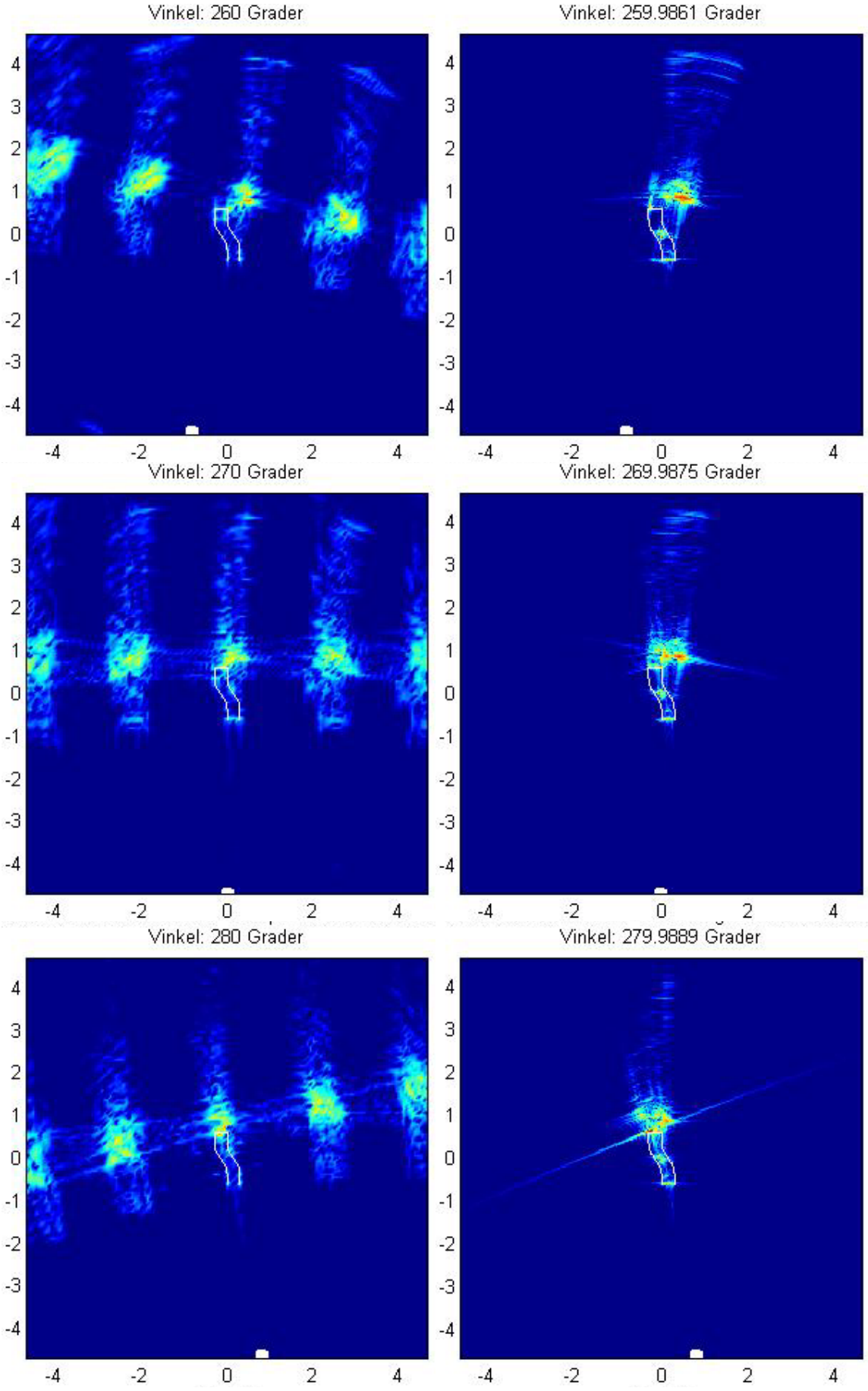
Vinkel: 260 Grader
Vinkel: 259.9861 Grader
Vinkel: 270 Grader
Vinkel: 269.9875 Grader
Vinkel: 280 Grader
Vinkel: 279.9889 Grader
4
3
2
1
0
-1
-2
-3
-4
-4
-2
0
2
4

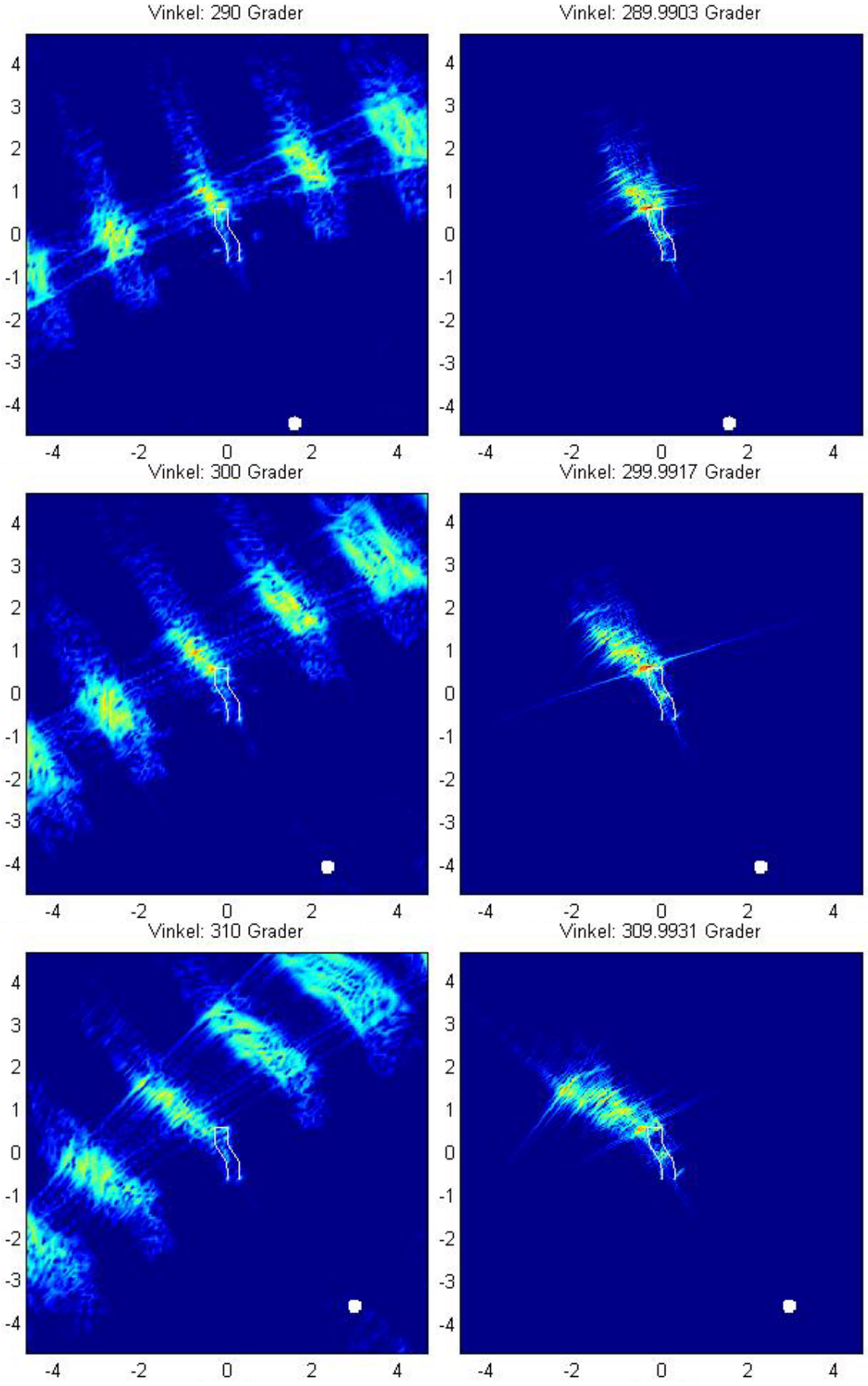
Vinkel: 290 Grader
Vinkel: 289.9903 Grader
Vinkel: 300 Grader
Vinkel: 299.9917 Grader
Vinkel: 310 Grader
Vinkel: 309.9931 Grader
4
3
2
1
0
-1
-2
-3
-4
-4
-2
0
2
4

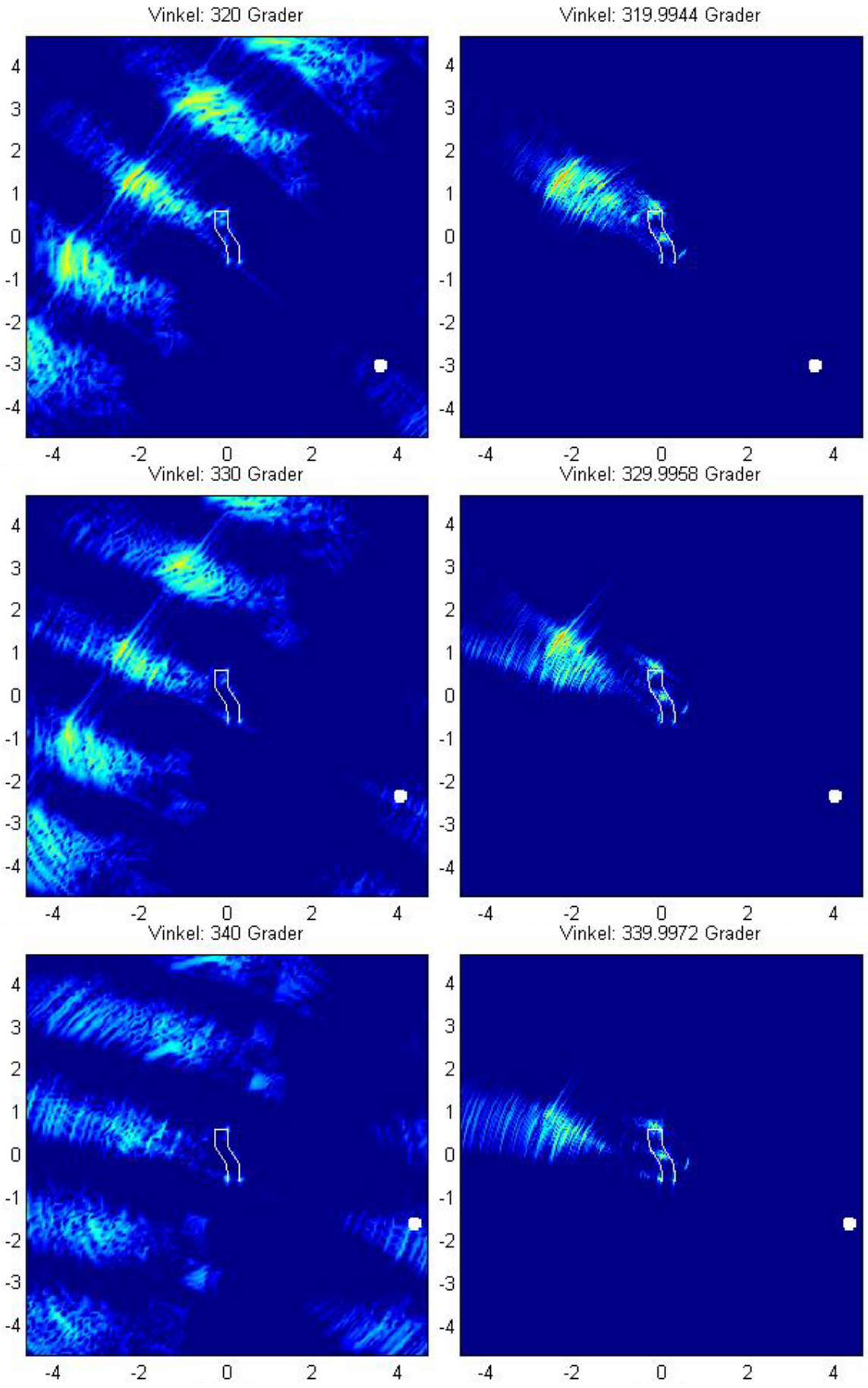
Vinkel: 320 Grader
Vinkel: 319.9944 Grader
Vinkel: 330 Grader
Vinkel: 329.9958 Grader
Vinkel: 340 Grader
Vinkel: 339.9972 Grader

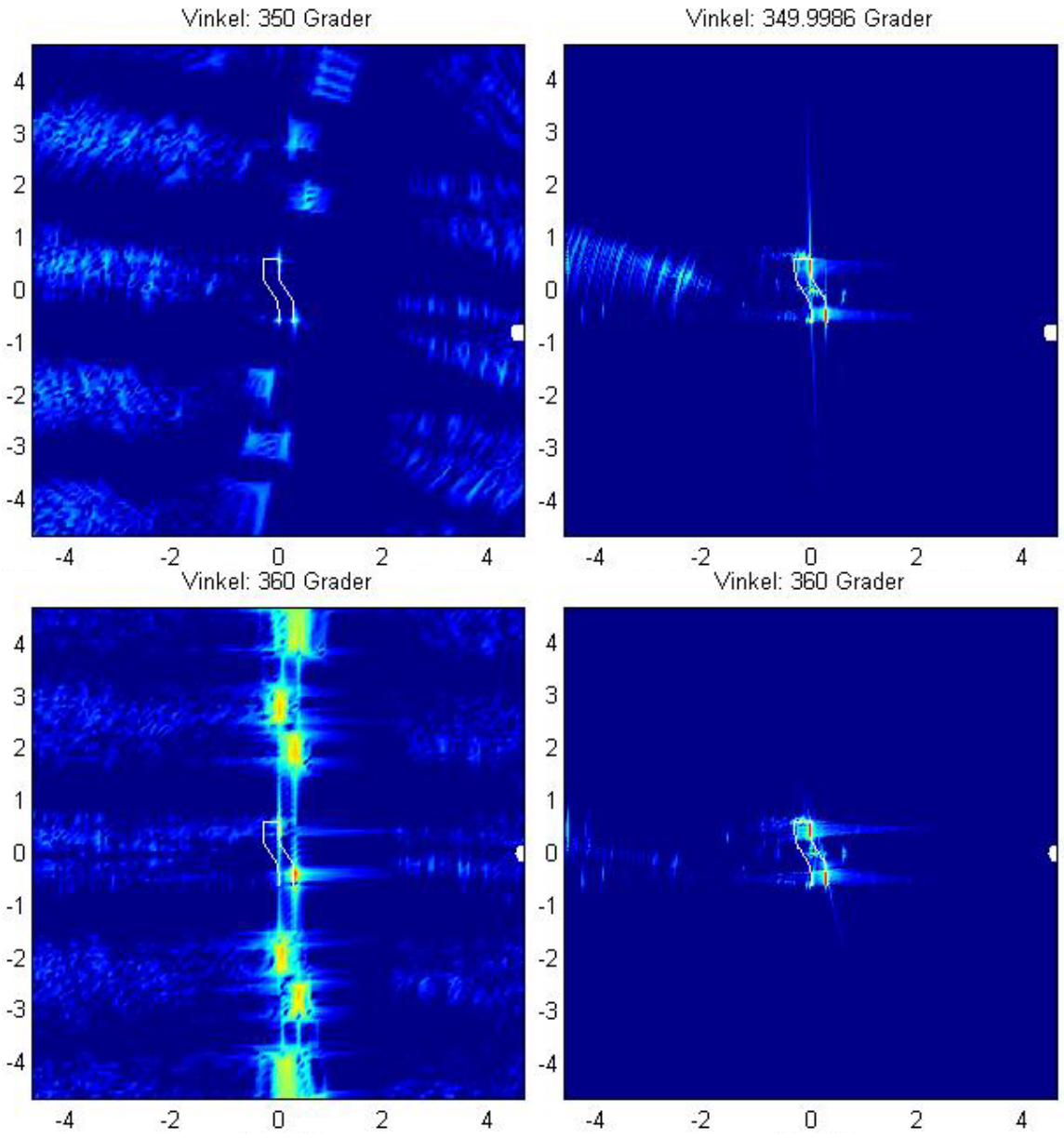
Vinkel: 350 Grader
Vinkel: 349.9986 Grader
Vinkel: 360 Grader
Vinkel: 360 Grader
4
3
2
1
0
-1
-2
-3
-4
-4
-2
0
2
4